REPORT DOCUMENTATION PAGE

Form Approved
OMB No. 0704-0188

Public reporting burden for this collection of information is estimated to average 1 hour per response, including the time for reviewing instructions, searching existing data sources, gathering and maintaining the data needed, and completing and reviewing this collection of information. Send comments regarding this burden estimate or any other aspect of this collection of information, including suggestions for reducing this burden to Department of Defense, Washington Headquarters Services, Directorate for Information Operations and Reports (0704-0188), 1215 Jefferson Davis Highway, Suite 1204, Arlington, VA 22202-4302. Respondents should be aware that notwithstanding any other provision of law, no person shall be subject to any penalty for failing to comply with a collection of information if it does not display a currently valid OMB control number. **PLEASE DO NOT RETURN YOUR FORM TO THE ABOVE ADDRESS.**

1. REPORT DATE (DD-MM-YYYY)	2. REPORT TYPE	3. DATES COVERED (From - To)
20-09-2004	Memorandum	2003

4. TITLE AND SUBTITLE

Water Mist Suppression of PMMA Boundary Layer Combustion – A Comparison of NanoMist and Spray Nozzle Performance

5a. CONTRACT NUMBER

5b. GRANT NUMBER

5c. PROGRAM ELEMENT NUMBER

6. AUTHOR(S)

Chuka C. Ndubizu,* Ramagopal Ananth and Frederick W. Williams

5d. PROJECT NUMBER

5e. TASK NUMBER

5f. WORK UNIT NUMBER
61-8244-A-4-5

7. PERFORMING ORGANIZATION NAME(S) AND ADDRESS(ES)

Naval Research Laboratory, Code 6180
4555 Overlook Avenue, SW
Washington, DC 20375-5320

8. PERFORMING ORGANIZATION REPORT NUMBER

NRL/MR/6180--04-8824

9. SPONSORING / MONITORING AGENCY NAME(S) AND ADDRESS(ES)

Office of Naval Research, Code 334
800 North Quincy Street
Arlington, VA 22217-5660

10. SPONSOR / MONITOR'S ACRONYM(S)

11. SPONSOR / MONITOR'S REPORT NUMBER(S)

12. DISTRIBUTION / AVAILABILITY STATEMENT

Approved for public release; distribution is unlimited.

13. SUPPLEMENTARY NOTES

*GEO-CENTERS, Inc., Arlington, VA

14. ABSTRACT

Water is a multiphase fire-suppressing agent and its transport and distribution pose additional challenges that necessitate research efforts. This report compares the effects of ultra fine water mist (~3 μm) and regular spray nozzle mist (~30 μm) on forced flow boundary layer combustion of PMMA plate, where mist was introduced with the incoming air. With the spray nozzles, burning rate downstream was enhanced due to spray-induced turbulence, which enhanced heat feedback rate to the plate in this region. Because of the higher heat feedback rate, the downstream achieves steady state burning rate faster with mist than without mist. On the other hand, the ultra fine mist has no induced turbulence and burning rate was suppressed everywhere along the plate due to mist cooling and dilution effects. Transient burning rate downstream lasts longer in this case due to the lower heat feedback rate. Flame extinguishment is by blow-off and larger spray droplets are most efficient in achieving that.

20041008 282

15. SUBJECT TERMS

Suppression; Chemical mechanisms, Halon 131

16. SECURITY CLASSIFICATION OF:			17. LIMITATION OF ABSTRACT	18. NUMBER OF PAGES	19a. NAME OF RESPONSIBLE PERSON
a. REPORT	b. ABSTRACT	c. THIS PAGE	UL	67	Frederick W. Williams
Unclassified	Unclassified	Unclassified			19b. TELEPHONE NUMBER (include area code) 202-767-2476

Standard Form 298 (Rev. 8-98)
Prescribed by ANSI Std. Z39.18

Naval Research Laboratory

Washington, DC 20375-5320

Water Mist Suppression of PMMA Boundary Layer Combustion – A Comparison of NanoMist and Spray Nozzle Performance

CHUKA C. NDUBIZU

GEO-CENTERS, Inc.
Arlington, VA

RAMAGOPAL ANANTH
FREDERICK W. WILLIAMS

Navy Technology Center for Safety and Survivability
Chemistry Division

September 20, 2004

CONTENTS

Water Mist Suppression of PMMA Boundary Layer Combustion - A Comparison of NanoMist and Spray Nozzle Performance.

1. INTRODUCTION

Recent research efforts in water mist fire suppression technology are driven by the need to find an environmentally friendly alternative to halogen-based agents, which have been shown to have adverse effects on the atmospheric ozone layer. Water is a multiphase agent and unlike its gaseous competitors, its transport and distribution imposes additional challenges and requires research efforts to make water mist system a contending alternative. In fires involving condensed fuels, especially solids and high boiling point liquids, water mist is particularly effective if the droplets can get to the condensed fuel surface and absorb latent heat of vaporization from the surface. In this way the surface is cooled directly and the burning rate is rapidly suppressed.

Most early studies of water mist fire suppression mechanisms and mist transport /distribution challenges, were conducted with pool fires and majority of them are large scale rather than laboratory scale. The earliest work was done by Rasbash et al [1] and they showed that water mist extinguishes liquid pool fires by gas phase cooling, oxygen dilution and surface cooling mechanisms. Downie et al. [2] studied the mist transport and distribution challenges in large fires. With the nozzle mounted above the flame, they showed that with large plume-to-spray thrust ratio, the penetration of the droplets into the fire region is negligible. Ndubizu et.al [3] studied the effects of droplet size and injection orientation on water mist suppression of low and high boiling point liquid pool fires. They made detailed temperature and burning rate measurement on 50-cm heptane and JP8 pool fires. Their measurements show that optimum suppression effectiveness is obtained with small droplets (~60 μm) injected at the base of the fire where a greater effect of oxygen dilution and heat absorption can be obtained. Finally they compared the suppression in liquid surface temperature and suppression in burning rate in tests with high flash point fuels (> 100°C) and showed that significant suppression is obtained when water droplets evaporate on the condensed fuel surface and cooled it directly. Kokkala [4] obtained similar results. He showed that with high flash point fuels (>100°C) the pool fire can be extinguished easily by cooling the surface with water spray but similar results were not obtained with low flash point fuels. In contrast, Mawhinney [5] observed intensified burning within the core of the flame in diesel pool fires when mist was injected from below. He attributed this to the effects of turbulence, which enhanced mixing and consequently the heat generation rate. These are rather qualitative observations. No quantitative measurements of enhancement in the large scale fires have been made.

In most laboratory-scale studies of water mist suppression mechanisms in diffusion flames, both in co-current [6] and countercurrent [7,8], configurations, water mist was known to suppress or extinguish the flame and the key mechanisms of suppression/extinguishment were identified as thermal cooling and oxygen dilution.

However there are a few surprises [9-11] where the introduction of a small amount of water droplets or vapor was suspected to enhance the burning rate instead of suppressing it. Atreya et al [11] ran experiments, where large water droplets were introduced on the surface of a methane ceramic burner. With a sooty methane flame, they observed an increase in heat release rate at low water application rates and suppression in heat release rate at high water application rates. However, they did not observe similar effects in a blue methane flame. To determine whether the enhancement is as a result of chemical effects or as a result of increased mixing due to the volumetric changes during droplet evaporation, they ran further experiments with methane counter-flow diffusion flame, where water vapor was introduced with the air. Their results show that as water vapor replaced nitrogen in the air, the heat release rate went up. This suggests that water vapor at low concentrations may enhance the combustion reactions in the gas phase. In a related study Richard et al [9] recently ran experiments with small heptane pool fires where the heptane was supported on a pool of water of equal volume. As the heptane burns the water underneath is heated to boiling by a hot plate. In this arrangement steam is introduced at the base of the flame where considerable chemical reactions take place. Their measurement in the exhaust gases show an increase in CO_2 concentration and a decrease in CO concentration with steam addition They also measured a decrease in soot formation. However when water vapor was replaced with nitrogen in this experiment similar effects were not obtained. They speculated that the enhanced oxidation is due to the so-called water gas reaction.

Very few studies have considered the water mist suppression of fire in boundary layer combustion configuration. Tamanini [12] studied the suppression of fire on burning vertical slabs using water mist sprayed horizontally on the fire. He obtained a power-law correlation between the burning rate and the water application rate. Earlier, Magee and Reitz [13] conducted similar experiments, where vertical and horizontal plastic slabs were subjected to turbulent burning with external radiation and horizontal water spray (for the vertical slabs). The "weighted" droplet diameters were about 1300 and 650 μm. They determined the critical conditions for extinguishments and showed that for plastics that do not melt excessively the primary mechanism for suppression is by surface cooling. In theses large-scale studies water is sprayed perpendicular to the wall fire and the droplets, especially the large ones have a greater chance of reaching the solid surface. In the current study, fine water droplets are mixed with the airflow upstream of a laboratory-scale boundary layer flame and detail local temperatures and burning rate were made to determine the effects of mist on the solid burning rate.

Recently, Ananth et al [14] and also Ndubizu et al. [15] have conducted detailed numerical and experimental studies of forced convection boundary layer combustion of polymethyl methacrylate (PMMA) plate. They considered laminar flow over a 7.5 x 9.5-cm sample without mist. By relaxing the assumptions in Emmons classical theory they obtained a modified relationship between dimensionless burning rate and Reynolds number Re_x which gives a better prediction of the burning rate at large Re_x. They also made detailed local temperature and time-averaged burning rate measurements along the length of the PMMA plate. Their results reveal that the local burning rate along the plate

2

is transient. In the leading section, the surface regresses rapidly after ignition leading to the formation of a small valley and a decrease in the heat feedback to the curved surface. As the valley deepens the local burning rate decreases. Downstream the heat feedback from the boundary layer flame to the surface is low and therefore it takes the solid considerable time to warm-up and to pyrolyze at a steady rate. Hence the burning rate increases as the solid warms up. In a similar configuration, Zhuo and Fernandez-Pello [16] studied turbulent burning of a small PMMA plate in forced convection. They showed a linear relationship between local burning rate and $Re_x^{0.5}$ and their results reveal that local burning rate increases significantly with turbulence intensity. In a related study, Ahmad and Feath [17] conducted a theoretical analysis of a turbulent wall fire without mist. They came up with an expression for local burning rate as a function of Raleigh number Ra_x, which fits their experimental data and that of some earlier works fairly well. Their results suggest that transition to turbulence influences burning rate but not very strongly.

Laboratory-scale study of water mist interaction with boundary layer flames is lacking. Recently, Sivathanu et al. [18] published a report on the effects of water mist on the rate of counter-current flame spread in a forced-flow boundary layer flame over PMMA. They used a 30 x 20-cm PMMA plate suspended at the middle of a wind tunnel. The flame position was tracked with a CCD camera. Water mist was injected into the airflow, 60 cm upstream from the flame and the spread rate was measured. Their results show that the spread rate decreases significantly with mist loading but the mist droplet size ($\sim$ 30 µm) had little effect on flame spread. They observed that the flame would rapidly extinguish when the spread rate decreases below $\sim$ 0.2 to 0.15 mm/min.

This work continues the study of the burning characteristics of a horizontal PMMA slab under a forced convection boundary layer flame. It focuses on the effects of water mist on the local burning rate of the PMMA plate. Water mist is injected into the wind tunnel from pressure atomizing nozzles and from an ultrasonic mist generator. Traditionally water mist is generated from spray nozzles but recently NanoMist Systems© LLC developed a technology for extracting very fine mist (NanoMist) generated from the ultrasonic vibration of piezoelectric discs [19]. NanoMist mean droplet diameters are of the order of 3 µm compared to about 20 to 100 µm for fine spray droplets. A detailed comparison of the performance of the two systems in boundary layer combustion of a PMMA plate is presented. We make detailed temperature measurements in the flame as well as local regression rate measurements and show that unlike with NanoMist, spray-induced turbulence enhances the burning rate downstream and aids in a quicker attainment of steady burning in this region.

3

2. EXPERIMENTAL

Figure 1 shows a schematic of the experimental setup, whose key components include the wind tunnel, the PMMA sample holder on an ATC® defense platform and thermocouples mounted on a set of Velmex X-Y unislides. The wind tunnel has a 36 X 45 X 61 cm plenum at one end into which an Ametek RJ054® variable speed blower pumps air. Pressure build up in the plenum drives the flow of the oxidizer through the wind tunnel and hence the effects of the blower on the flow are minimized. Wind velocity (U) in the tunnel is selected by adjusting the speed of the blower. A 30-cm converging section connects the plenum to the straight section, which has a 15-cm X 15-cm cross section. A set of fine screens are placed at the entrance and exit of the converging section and a 3mm honeycomb, 2.5 cm thick is inserted after the converging section to smooth the flow. Mist is introduced into the airflow after the honeycomb in a small removable chamber with the same cross-sectional area. The mixture of air and water mist flows through the remaining 90-cm section of the tunnel to the exit, where the burning PMMA plate is located.

As the air flows over the burning PMMA plate, a boundary layer flame is formed. The location of the boundary layer flame at the exit instead of inside the tunnel has two advantages. First, we have easy access to move thermocouples in and out of the boundary layer flame to map temperatures. Secondly, we avoid water dripping on the burning surface from the wind tunnel ceiling, which would taint the results. The PMMA samples (7.5 x 9.5 cm) are made from Cyro® Acrylite GP sheet nominally 2.54 cm thick. The samples were milled to a thickness of 2.3 cm. The choice of sample thickness is influenced by the experiments of Vovelle et al. [20] and also Tewarson and Pion [21], which showed that the initial sample thickness does not affect the burning rate if it is larger than 1.5 cm. Detailed discussion of the experimental setup and the design of the sample holder was given elsewhere [15].

Five R-type thermocouples, 50 μm (0.002") in diameter, are mounted on the Velmex® X-Y unislides. The unislide motors are computer controlled by a Velmex® NF90 controller such that the thermocouples can be placed precisely at any point in the middle plane of the flame. Voltage signals from the thermocouples are passed through the National Instruments'® TC 2095 terminal block into the SCXI 2000 chassis where the signals are conditioned and digitized. LabView software is used for motor control as well as continuous temperature data acquisition.

2.1 Mist Generation

The experimental setup was designed to accommodate mist injection into the air stream using nozzles and the ultrasonic mist generator (UMG). With nozzles a single (or multiple) pressure-atomizing nozzle PAN was positioned at the center of the mist generation section (Fig. 1) and mist is injected co-currently with the airflow.

4
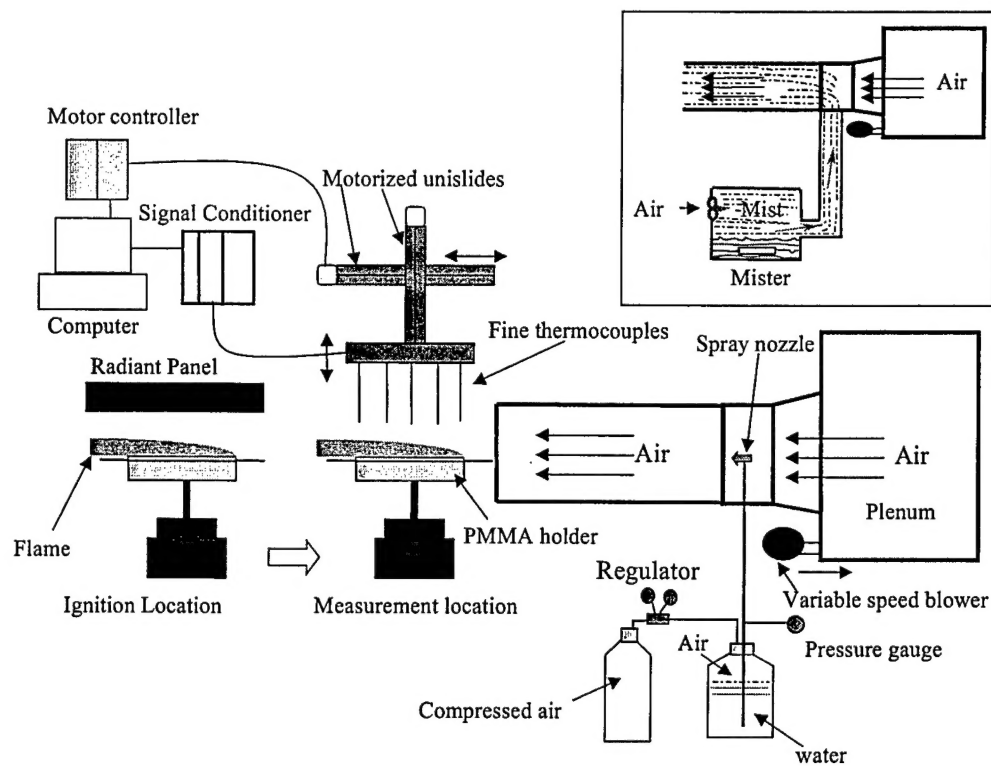
Figure 1: Schematic of the test setup with pressure atomizing nozzle and with NanoMist (Insert top right corner)

A 30-cm long mist generation section (Fig. 1) was used with nozzles and a 60-cm long section was used with the UMG. A shorter length was used with the nozzles in order to minimize mist losses on the tunnel. Two types of nozzles were used. Delavan's WDB® nozzles were used to produce solid cone sprays with relatively larger droplets (~40 μm), while Atomizing Systems'® impingement-pin nozzles were used to produce smaller droplet sprays (~15 μm). Picture of the two types of nozzles is shown in the Appendix, Fig. A1. Bottled compressed air is used to pressurize distilled water in a ~ 9.4-liter tank and force it through the spray nozzle placed at the center the mist generation chamber (Fig. 1). A steady mist flow rate is obtained by keeping the pressure constant using a Matheson 3030® pressure regulator.

Ultra fine mist was produced with an Ultrasonic Mist Generator (UMG) made by NanoMist Systems LLC. Here, mist is generated by the ultrasonic vibration of piezoelectric discs under water. For the purpose of our discussions the mist from the NanoMist Systems generator will be called NanoMist. A small fan is used to extract and inject Nanomist at the floor of the wind tunnel. The insert at the top right corner of Fig. 1 shows the setup when NanoMist is used. The NanoMist droplets are very fine and they follow the streamlines. Therefore mist losses are less and a longer generation section (60 cm) could be used. The longer mist chamber helps dampen the effects of mist injection cross flow (Fig. 1 insert).

2.2 Test Procedure

In tests with PANs, the nozzle is setup in the mist generation chamber and the air pressure is set in the water tank. The blower is turned on and adjusted to produce a velocity at the exit of the tunnel (measurement location) as measured by a hot wire anemometer. The velocity profile across the tunnel without mist is relatively uniform near the center and it is taken as the free stream velocity U_∞. In tests with NanoMist the contribution of the mist extracting fan is taken into account in determining the air velocity in the wind tunnel. Thus in these tests the small fan is turned on without energizing the piezoelectric discs and then the blower is turned on and adjusted to obtain the desired velocity. With the $U_\infty = 84$ cm/s, the fan contributed about 30% of the total airflow.

In mist experiments, the mist is turned on as the entire sample surface is uniformly heated and ignited under a radiant panel 40 cm downstream from the tunnel exit (Fig. 1). The process of irradiation, surface gasification and the establishment of a stable 2-D flame over the sample, take place in about 40 seconds. This gives time for the mist flow to attain steady state. Time is started immediately after ignition. Thereafter, the burning sample is quickly moved to the measurement location at the tunnel exit. Gas phase temperatures are measured simultaneously at five X locations with five thermocouples. The sample is allowed to burn for a known time interval before the flame is extinguished. The mist flow is then turned off. After the sample cools, its thickness along the centerline is measured at various X locations with a digital micrometer whose accuracy is ±0.003 mm. Since the initial thickness of the sample was measured, the sample regression rate at each location is obtained as the difference in thickness, after

correction for PMMA thermal expansion [15, 22] divided by the test duration. Detailed discussion of the errors and corrections in the regression rate was presented in our earlier paper [15].

2.2.1 Temperature Measurement

Although surface regression is not uniform along the sample length, the highest regression rate as we shall present later is ~1 mm/min. If the flame moves down at that rate, it is necessary to complete the temperature mapping across the flame in less than 1 min to avoid significant errors in the measurement. At the same time it is necessary to allow enough time ($\geq$ the thermocouple time constant) during each measurement for the thermocouple bead to attain thermal equilibrium with the surrounding gases. For a 50-μm diameter butt-welded thermocouple the bead diameter is about 125 μm and the time constant is approximately 30 ms [23]. Since the temperature gradient is very large within the boundary layer, measurements need to be made at very short distance intervals and we chose 0.5-mm intervals. The thermal boundary layer is ~10 mm in the trailing section. Therefore, approximately 25 measurements at 0.5-mm intervals were made across the flame at each X location to map the temperature within the boundary layer. To map the temperature across the flame in less than 1 minute, the data acquisition system was programmed to acquire data at the rate of 20 per second and 20 data samples were averaged per recorded temperature value. With the travel time of the thermocouple and the processing time, the temperature mapping across the entire flame was completed within 45 seconds.

Each averaged temperature datum has an error, which varies with location in the flame. In the base case test, the error is of the order of ±40K near the peak temperature location. Above the peak location toward the free stream, the error is higher because of instabilities. However, below the peak location toward the sample surface the error decreases below ±40K. Indeed, it is about ±10K in the molten region. Generally the error is least in the leading section and highest (about ±150K) in the plume zone near the trailing edge, where buoyancy and other externally induced disturbance effects are significant and the flow fluctuates much more.

Since the thermocouple wires are crossing regions of high temperature gradients, the measurements are expected to include conduction errors. To minimize this error we chose very fine thermocouples with diameter of 50 μm. The conduction error with these thermocouples is expected to be small since the conduction heat transfer area (the cross-sectional area of the thermocouple) is very small. No corrections were made in the data for conduction errors. However, the temperature values are corrected for thermocouple bead radiation loss and the details about the correction are given elsewhere [6]. For the 50-μm-diameter thermocouple a typical radiation correction at 1800 K is +62K.
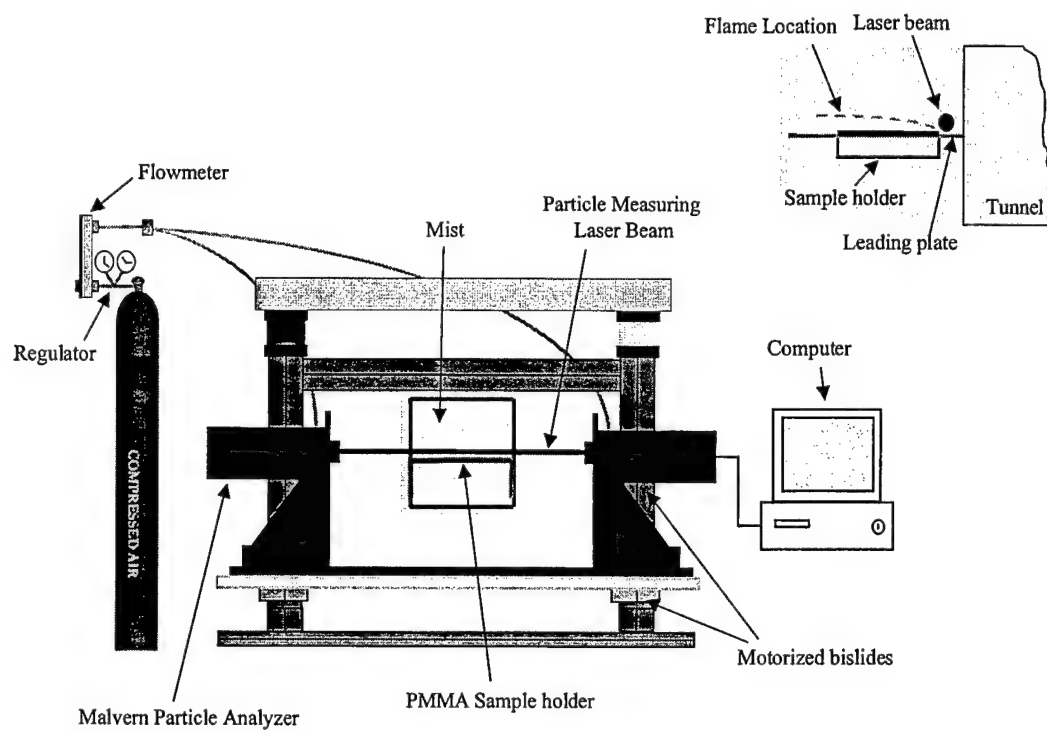
2.3. Mist Characterization

Separate experiments were conducted to characterize the mist. Mist characterization measurements were made with Malvern Instruments' Spraytec® particle size analyzer and the parameters were measured dynamically as mist flows over the small PMMA plate at the measurement location without the flame over it. This ensures that light emitted from the flame does not taint the results. The instrument is mounted on a pair of Velmex® X-Y bislides at the exit of the wind tunnel such that laser beam passes through the mist cloud over the leading plate near the sample upstream edge (Fig.2). With the computer-controlled bislides, the instrument can be moved in the stream-wise or vertical direction to make measurements above the sample and along the length of the sample. The Instrument has a 5mW He Ne laser with a wavelength of 670 nm. We used the 10 mm diameter laser beam. Most of the measurements were made with the center of the beam ~5 mm from the plate surface (Fig. 2 insert). This ensures that the section of the mist approaching the flame location is intersected by the beam. Recall that the flame maximum thickness near the trailing edge is ~10 mm. The signal from the transmitter is scattered and attenuated as it passes through the mist cloud and the resultant signal is received at the receiver. The Malvern Real Time Particle Sizer software is used to obtain droplet size distribution and volume concentration with time. The software also gives a time-averaged droplet diameters and concentration in parts per million. The Sauter mean diameter is the diameter of interest here since it is defined in terms of the droplet surface area, which is a key parameter that determines droplet heat and mass transfer rate.

The Instrument was calibrated in the factory and also calibrated on site using NIST-traceable reticles. The results are given in terms of diameter distribution in the Appendix, Fig. A2. The tests reported here were conducted at the same inlet velocity U_∞ as was used in the combustion experiments. U_∞ was 84 cm/s for all PAN tests.

In tests with PANs, mist loading was varied by varying the pressure for a given nozzle, using more than one nozzle at a given pressure or using a different type of nozzle. With the NanoMist, on the other hand, mist loading was increased by increasing the number of piezoelectric discs that are energized or by reducing the inlet air velocity. Mist mass loading was calculated using the Spraytec® concentration data. This gives the concentration of liquid water in the flow. We also calculated mass loading from mist flow rate measurements. With the PANs the mist flow rate F_p for the various nozzles at every pressure of interest was first measured outside the tunnel by weighing the water sprayed into a container within a known time. During the mist characterization tests we collected and weighed the water deposited on the walls of the tunnel and that drained out of the tunnel. Thus, the mist loss rate F_l is obtained and the air-borne mist flow rate at the exit of the tunnel is F_p- F_l. Finally, with the air-borne water flow rate and the known airflow rate, the mist loading is calculated. In tests with NanoMist, the mist output rate F_m is obtained by measuring the change in volume of the pool of water over the piezoelectric discs within the test time. The mist loading is obtaining using the airflow rate and F_m - F_l. This mass loading includes contribution from water vapor.

Figure 2: Schematic of the mist characterization setup. Insert at the top right corner shows the location of the laser beam relative to the flame location

As the piezoelectric discs in the UMG vibrate they heat up the pool of water. This decreases the surface tension of water and makes atomization easier. Hence, the mist concentration increased with time in NanoMist tests. Therefore, the NanoMist data (SMD, mass loading) are time-averaged values for the length of time the experiments lasted. With the pressure atomizing nozzles (PANs) the water temperature does not vary with time and mist concentration does not vary with time.

3. RESULTS AND DISCUSSIONS

3.1 Mist Characterization Results

Table 1 presents the pertinent parameters of the various nozzles used in the experiments. These include the orifice diameter, the test pressure, the measured mist flow rate at the test pressure and a short identification of each nozzle experiment to be used in the rest of the discussions. The mist flow rate in Table 1 was measured outside the wind tunnel. In the experiments, mist was injected co-currently into the tunnel airflow in the mist injection compartment (Fig.1). As the mixture of air and mist flow to the exit of the wind tunnel some mist is lost to the walls of the tunnel due to collision with the walls or due to the effects of gravity.

Table 2 presents the mist characteristics measured with Malvern Instrument's Spraytec® at the exit of the tunnel just before the flame (Fig. 2 Insert). The characterization tests were conducted at the same U_∞ that the combustion tests were conducted. The droplet distribution histograms are shown in the Appendix, Figs. A2 and A3. Peak volume frequency is a measure of the highest fraction of the total water volume made up of droplets of a given diameter. With the PANs, it varied between 15.6% and 8.6% while the diameter at the peak volume frequency varied between 63 and 24μm. The Sauter mean diameter SMD varied between 47 and 11μm. The solid cone nozzles produced larger diameter droplets than the impingement pin nozzles, which were run at higher pressures. The pin in front of the nozzle orifice also helps in further breakup of the droplets. With Nanomist the SMD was ~3 μm, the peak volume frequency was 7.8 and the diameter at the peak volume frequency was 7.9 μm.

The Spraytec data for droplet concentration is given in parts per million and the data is converted to mist mass loading, which is presented in Table 2. This mass loading varied between 0.44% and 1.48%. It is pertinent to note that the mist injection rate into the wind tunnel from the SC1 nozzle and the UMG are about equal 49 gm/min and 47 gm/min respectively. However the nozzle spray has a much higher mean droplet diameter compared to the ultra fine mist, 47μm to 3μm. Hence the ultra fine mist is easily carried by the airflow unlike the large droplets. Therefore mist losses are much higher with the nozzle and the mist loading as measured by the Malvern Spraytec is much lower with the nozzle than with the UMG. The values are 0.44% for SC1 nozzle and 1.6% for the NanoMist. More detailed discussion of mist transport through the tunnel is presented later.

10

Table 1 Parameters for the pressure atomizing nozzles

Nozzle make and Type	Orifice diameter (mm)	Pressure (Kg/cm^2)	Mist flow rate at nozzle exit (cc/min)	Nozzle Identification
Delavan WBD 1.5 Solid cone	0.33	2.81 (40 psi)	48.8	SC1
Delavan WBD 1.0 Solid cone	0.28	5.27 (75 psi)	42.7	SC2
Delavan WBD 1.0 Solid cone	0.28	3.5 (50 psi)	36.1	SC3
Delavan WBD 0.5 Solid cone	0.21	70.3 (100 psi)	24.28	SC4
2 Spray systems 004 Impingement pin	0.10	210.9 (300 psi)	43.72	IP1
Spray systems 004 Impingement pin	0.10	281.2 (400 psi)	25.5	IP2
Spray systems 004 Impingement pin	0.10	456.95 (650 psi)	32.45	IP3
Spray systems 006 Impingement pin	0.15	5.27 (75 psi)	25.1	IP4

Table 2 Measured Mist parameters

| Nozzle Identification	Diameter at peak volume frequency (μm)	Peak Volume Frequency (%)	Sauter Mean diameter (μm)	% Mist mass loading (measured)	% Mist mass loading (Malvern)
SC1	63	12.9	47.35	1.4	0.44
SC2	54.86	13.32	39.7	1.0	0.7
SC3	54.86	12.75	43.14	0.44	0.47
SC4	36.24	13.82	28.25	1.1	0.49
IP1	27.49	11.29	16.4	1.6	1.04
IP2	23.94	10.15	13.2	1.7	1.23
IP3	18.16	8.79	10.09	2.2	1.48
IP4	47.78	15.6	38.28	0.85	0.64
NanoMist	7.92	8	3.15	2.5	1.04
NanoMist	7.9	7.8	3.16	4.3	1.6

Also shown in Table 2 are the mass loading values calculated using the mist output at the generation point, mist losses before the flame and the total air flow rate. The values of the mass loading measured this way varied between 4.3% in NanoMist and 0.44% in SC3. In each test the mass loading calculated from our measurements are higher than that calculated from Spraytec measurements. With Nanomist mist evaporation rate is quite high since the droplet diameters are very small and the difference between the two mass loading value would be due to water vapor. Indeed, the contribution due to water vapor is highest with NanoMist, ~ 2.7%. Incidentally, at ambient conditions the saturation water mass loading is ~2.3%. It is therefore likely that the air in the Nanomist tests is saturated with water vapor.

3.2 Effects of Mist on the Flame Temperature

With the pressure atomizing nozzles, the nozzle is positioned at the center of the tunnel at the mist generation section and mist is sprayed co-currently into the tunnel airflow. The injection action is expected to disturb the airflow, despite the co-current arrangement. The disturbance would propagate downstream and could eventually affect the boundary layer flame at the exit of the tunnel. This could cause fluctuations in the flame that are expected to increase with U_∞ and X (Re_x).

To investigate the effects of instabilities induced in the tunnel by mist injection we measured the variation in flame temperature with time at various points in the flame in tests with and without mist. The measurements were made at Y = 4, 8 and 12 mm and X = 22, 37, 57 and 78 mm. X is the distance from the upstream edge of the plate and Y is the height above the sample surface before ignition. Some of these points are on the fuel side and some are on the airside of the diffusion flame. A typical result for a test with the thermocouple at a downstream location X = 57 mm, Y = 8mm is shown in Fig. 3. This point is on the airside of the diffusion flame but close to peak temperature location. Figure 3 presents 100 temperature data (20/second) for the base case and four PAN mist cases. Also included for comparison are data from tests with nitrogen and NanoMist. As expected the measured temperatures with mist are lower that those without mist due to the cooling effects of mist. Compared to the base case and the nitrogen data the results with PAN show a much larger scatter, which depicts the effects of flow fluctuations in the flame. For example, while the base case data varied within <50 K, the SC2 data varied within 500 K. Indeed, significantly higher flame fluctuations were observed visually in tests with nozzles. The data with NanoMist show the effects of small flow instability caused by the cross flow (see insert in Fig. 1). NanoMist is generated outside the tunnel in the mister. It is extracted with an air flow from a small fan and carried into the tunnel through a 15-cm diameter hole on the floor of the wind tunnel. Recall that the wind tunnel cross section is 15 x 15 cm and so the mist inlet opening is large to reduce the cross flow velocity. We also provided an extra 60 cm length of mist chamber to dampen the effects of the disturbance from the cross flow. Despite these precautions the effects of the cross flow are not entirely eliminated. However, this disturbance is less than that induced by the pressure atomizing nozzles. The flow disturbance induced by the mist
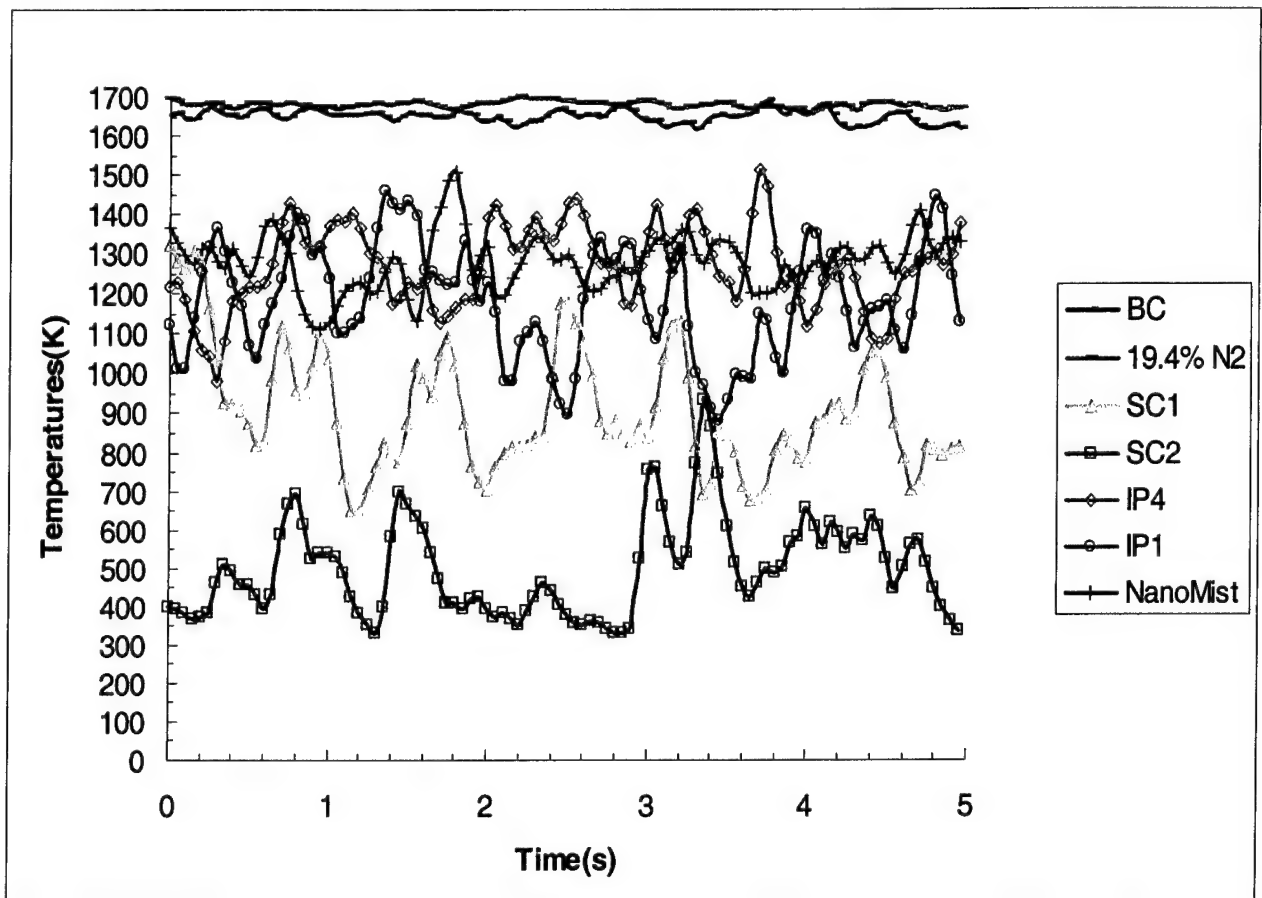
Figure 3: Temperature variation with time at X = 57 mm Y = 8 mm (near the peak temperature location) in the base case test and tests with N_2, SC1, SC2, IP1, IP4 and NanoMist

spray action is expected to affect the burning characteristics of the PMMA plate and this will be discussed later. First, we present the effects of NanoMist, which induced minimal disturbance on temperature profiles.

### 3.2.1 Effects of NanoMist on Local Temperature Profiles

Figures 4 a and b show the pictures of NanoMist cloud flowing over the PMMA plate before ignition and after ignition, respectively. The mist mass loading in this case is 4.3% (1.6% with Malvern). Visually one can see that both the mist flow and the flame are laminar. Temperature mapping was initiated after the ignited sample was moved to the exit of the tunnel and the flame had stabilized. The measurements were completed within the second minute after ignition.

Figures 5 and 6 compare the temperature profiles at various stream-wise locations in tests with and without (base case) NanoMist and U_∞ = 84 cm/s. In Fig. 5 the mist loading is 2.5% (1.04%) and in Fig. 6 it is 4.3% (1.6%). The X locations are shown in the legend and the solid symbols represent base case while open symbols represent mist data. At each X location the temperature profile is expected to be dome-shaped, increasing with height Y on the fuel side of the flame, reaching a peak at the flame location and decreasing with Y on the airside. Figures 5 and 6 show that the dome shape could not be completed at some X locations. In the leading section this is due to surface regression. Recall that height above the sample refers to the height relative to the PMMA sample surface before the flame was ignited and the surface began to regress. The first and second thermocouples, which were 13 & 22 mm from the leading edge, could not reach the surface of the sample in this location since the surface had regressed a very small distance before the data was taken. Recall that the temperature gradient is very steep in this section and the change in temperature within a gap created by a one-minute regression can be significant. Therefore, Y = 0 represents the molten surface more appropriately at large values of X. In the trailing section the dome could not be completed because the thermal boundary layer thickness is larger in this section and only 25 measurements were made in the Y direction in order to complete the temperature mapping in under 1 minute as we discussed in earlier sections.

Both Figs. 5 and 6 show that NanoMist suppressed flame temperature on the airside of the diffusion flame but not on the fuel side. The suppression is due to the cooling effects of the evaporating droplets. The cooling effect is more in the leading section than downstream. NanoMist droplets are small with SMD ~3μm and therefore the droplets tend to follow the streamlines. Because they are that small they probably evaporate before they get to the flame front because the evaporation rate is fast as a result of the d^2 law. This explains why the reduction in temperature is only on the airside and minimally on the fuel side. It is also consistent with the result that temperature reduction is more in the leading section than down stream. For example in Fig. 6 the reduction in flame temperature at X = 13 mm Y = 4 mm is from ~000K to ~350K but the reduction in temperature at X = 79mm Y = 12 mm is negligible. A comparison of Figs. 5 and 6 shows
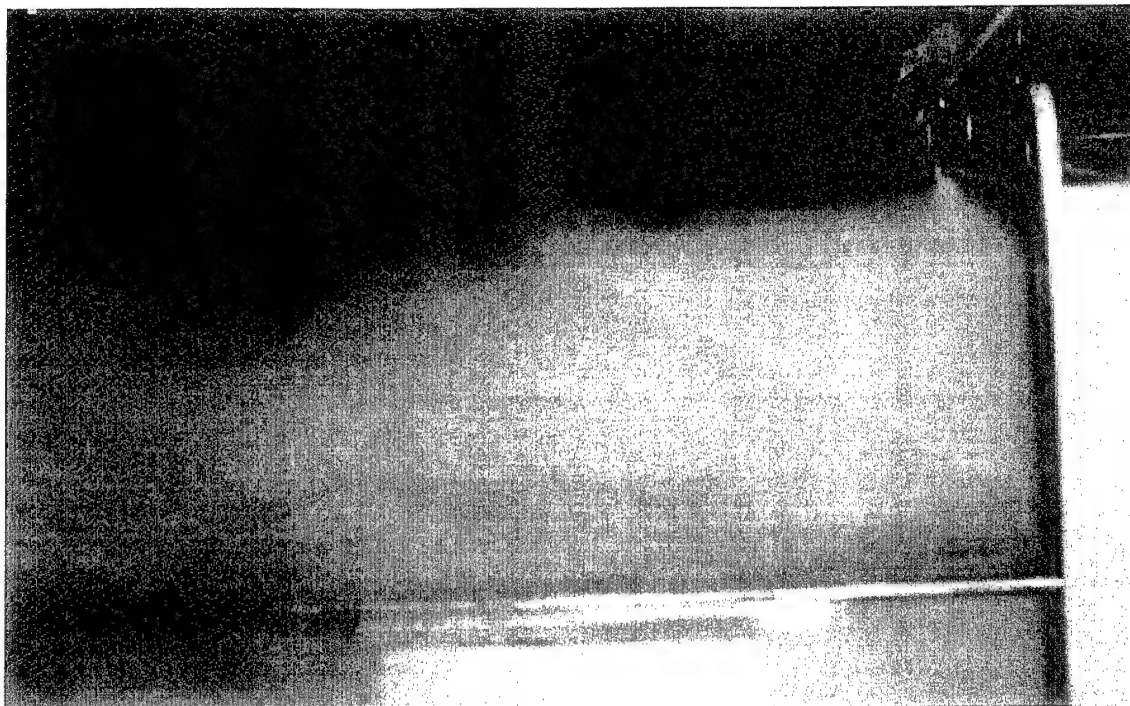
(a)
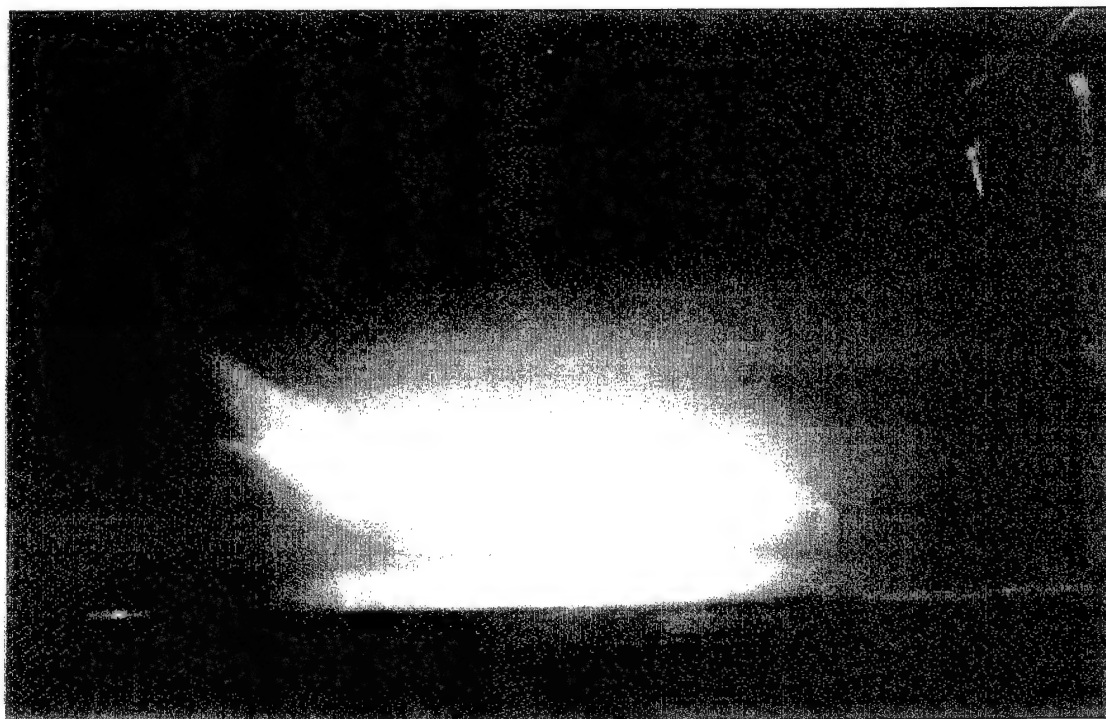
(b)

Figure 4: Picture of NanoMist flow over the PMMA plate at the tunnel exit. Mist mass loading = 4.3%, U_∞ = 84 cm/s (a) no flame (b) with flame
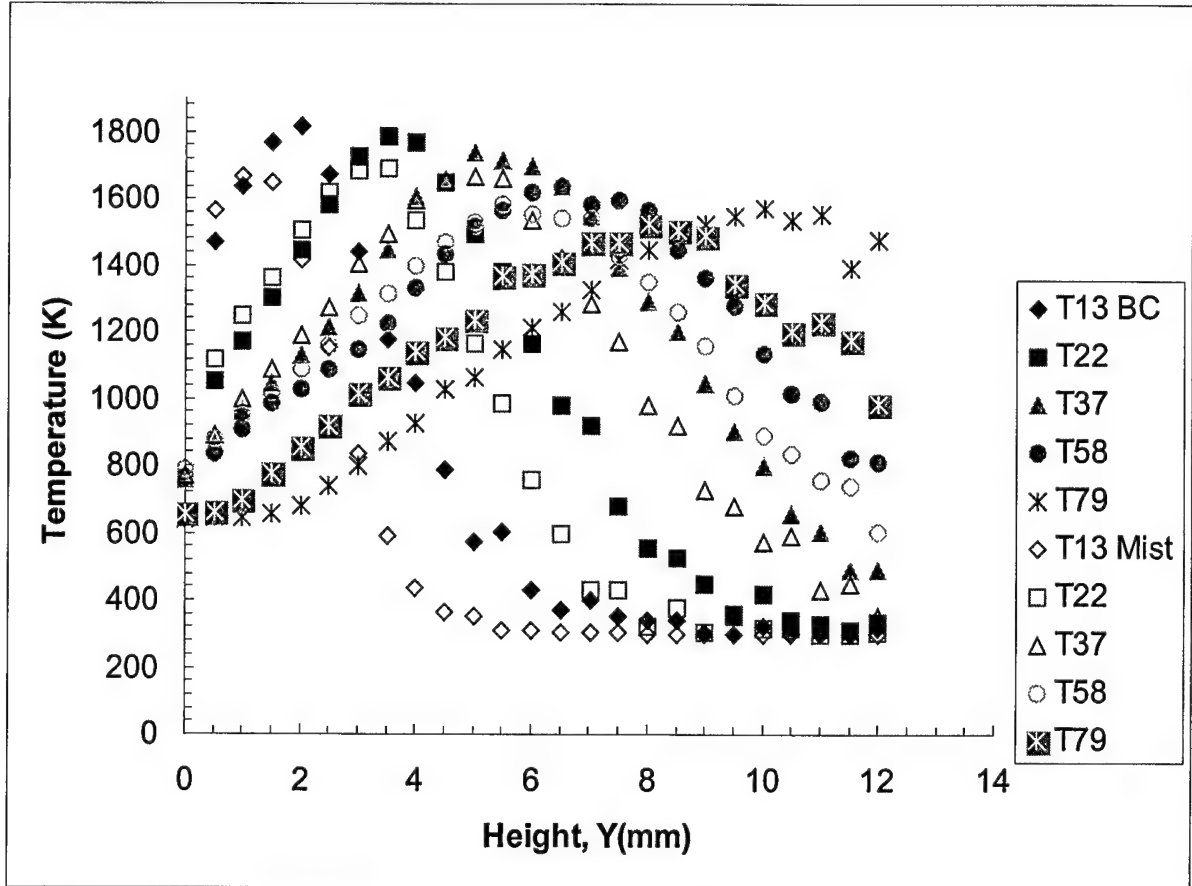
Figure 5: Temperature profiles along the PMMA plate, 13, 22, 37,58 & 79 mm from upstream edge. Base case and 2.5% NanoMist mass fraction $U_\infty = 84$ cm/s.
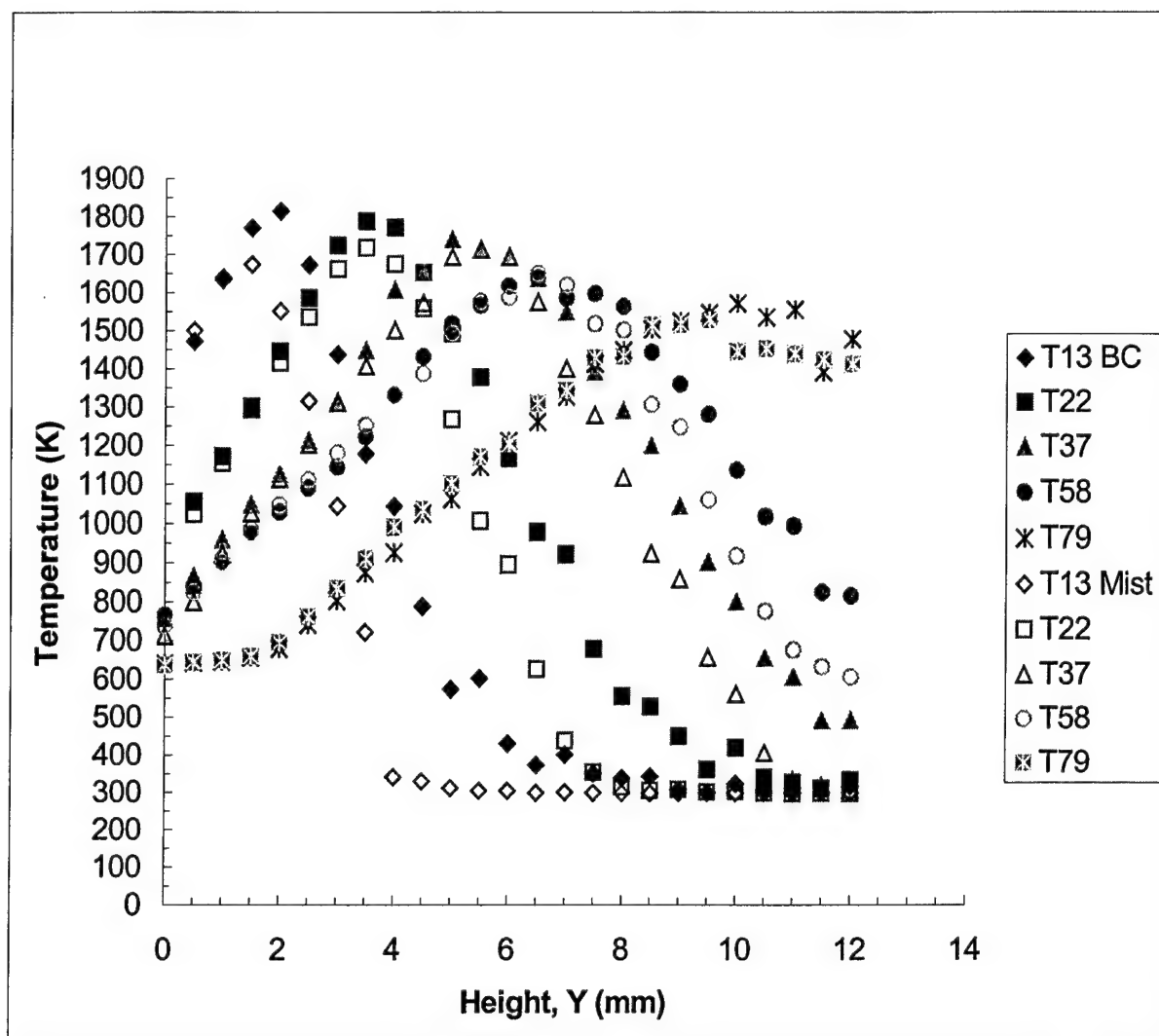
Figure 6: Temperature profiles along the PMMA plate, 13, 22, 37,58 & 79 mm from upstream edge. Base case and 4.3% NanoMist mass fraction, U_∞ = 84 cm/s.

that the effects of water mass loading 4.3% and 2.5% on the flame temperature is negligible. Because of the rapid cooling in the leading section we could not run the test with higher mass loading at 84 cm/s without the flame extinguishing by blowing off. Tests with lower mass loading showed little or no suppression. The suppression window is very narrow.

3.2.2 Effects of Mist from PAN on the Local Temperature Profiles

As presented in Fig. 3 the effect of spray-induced turbulence affects the flame especially down stream. We visually observed the highest flame fluctuation in tests with pressure atomizing nozzles. Figure 7 shows a picture of a typical flame in a test with pressure atomizing nozzle. It shows the high level of disturbance, especially downstream, unlike in Fig. 4 with NanoMist. Also shown in Fig. 7 is a short quench zone near the plate leading edge. As the flame was moved from the ignition location to the measurement location (Fig. 1), a quench zone was formed in the leading section due to the rapid cooling from mist. This cooling led to a decrease in the local Damkohler number (Da = flow time/reaction time) by increasing the reaction time. The flame anchors upstream from the leading edge, stabilizes and slowly spreads upstream. We had shown in an earlier paper [22], that this unexpected upstream flame-spread is facilitated by the effects of moving boundary. The quench distance in the tests with pressure atomizing nozzles range from about 2 mm to about 25 mm.

Figure 8 shows a temperature profile in SC1 test compared with the base case. In this test the first thermocouple (X=12mm) did not measure any high temperatures because it was in the quench zone and there was no flame there while the measurements were being made. The key point to be made with Fig. 8 is that the SC1 profile show more fluctuation than the base case especially for downstream locations, X= 57 mm and 78 mm from the upstream edge. These correspond to large Re_x locations. $Re_x = U_\infty X/\nu$, where ν is the kinematic viscosity of the ambient air. Recall that the PMMA plate is 95 mm long and $U_\infty = 84$ cm/s in these tests. In 381 x 127 mm wall fire experiments [24] it was observed that transition to turbulence regime begins for about $Gr_x > 0.5 - 2 \times 10^8$. Since $Gr_x^{0.25}$ is equivalent to $Re_x^{0.5}$ in forced convection, this could be equivalent to $Re_x^{0.5} > 50$ in forced flow. Indeed, $Re_x^{0.5}$ is approximately 50 for X=57 mm in the current tests.

For clarity the comparison of temperature profiles in tests with nozzles and the base case data are presented at 4 separate X locations, 22, 37, 57, and 78 mm from the upstream edge. Figure 9 shows temperature profiles at X = 22 mm. At this location, the thermocouples did not reach the molten surface to measure its temperature in most of the tests because of the quench zone and/or high regression rate as outlined earlier. The solid symbols are the base case data, while the open symbols are PAN mist case data. Also shown in the Figure are results in tests with additional nitrogen N_2. The N_2 data show a case where we have a large quench zone (~20 mm) in the leading section but without the
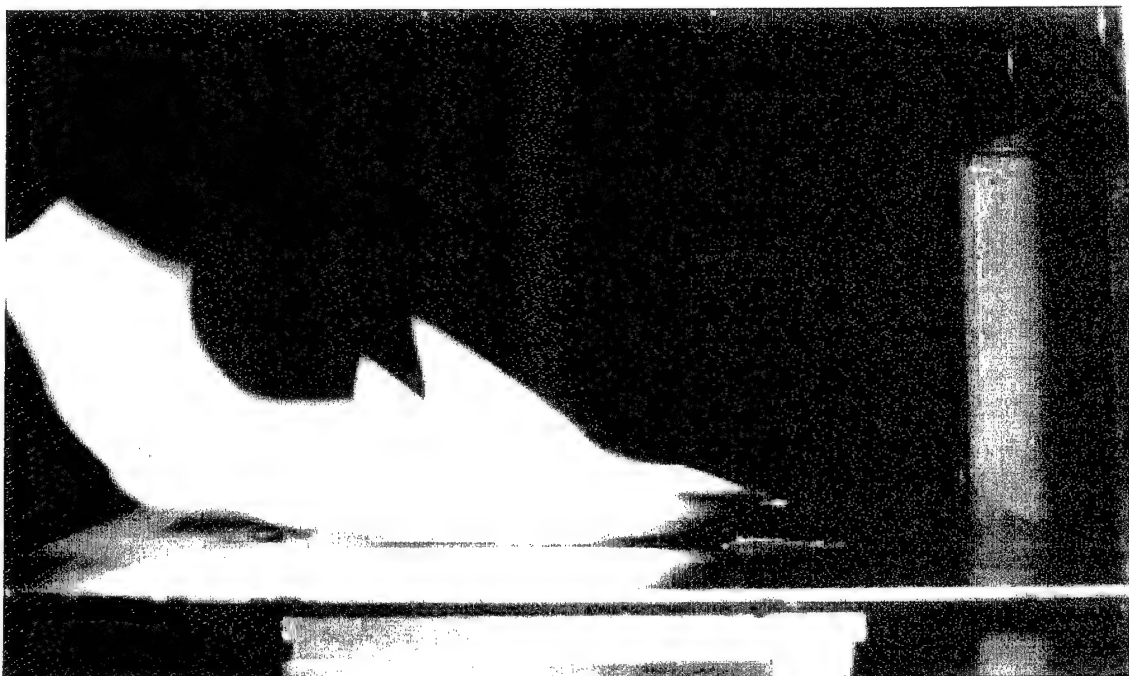
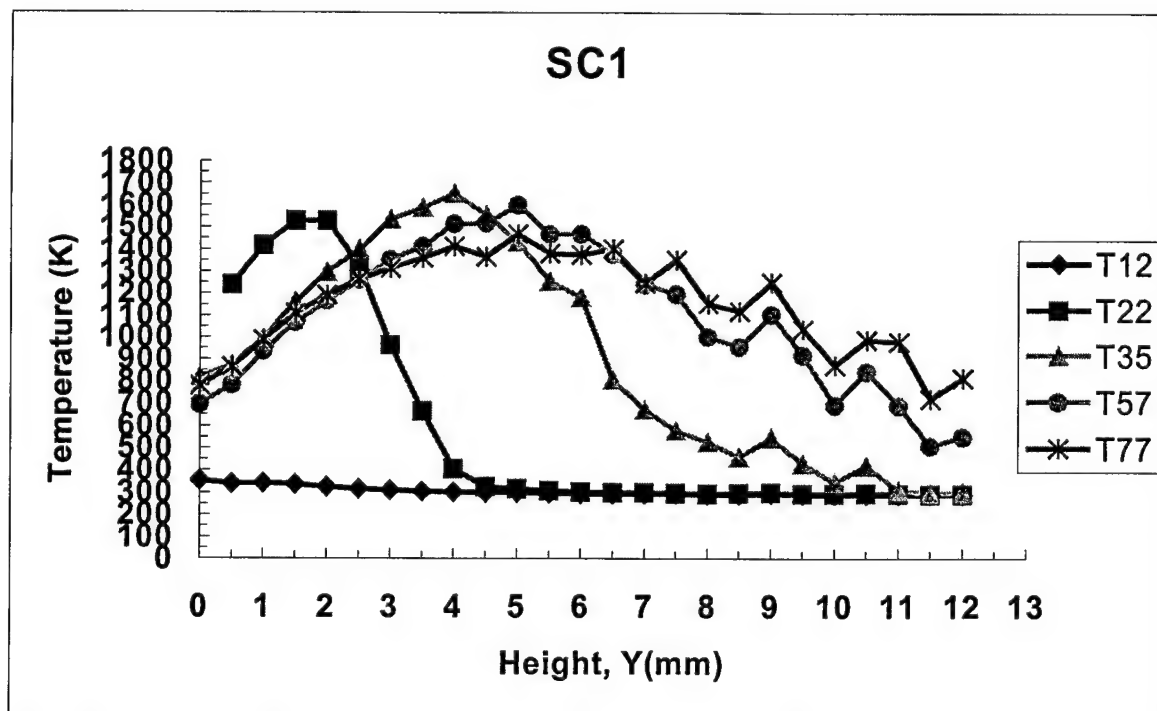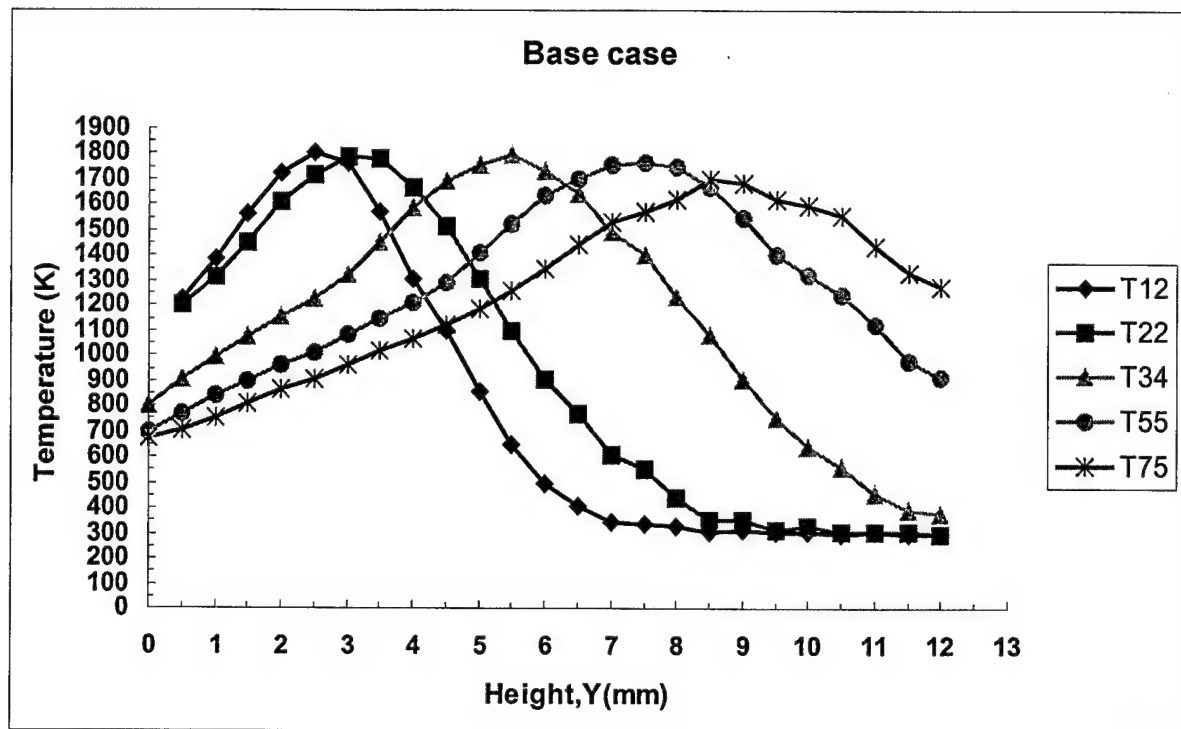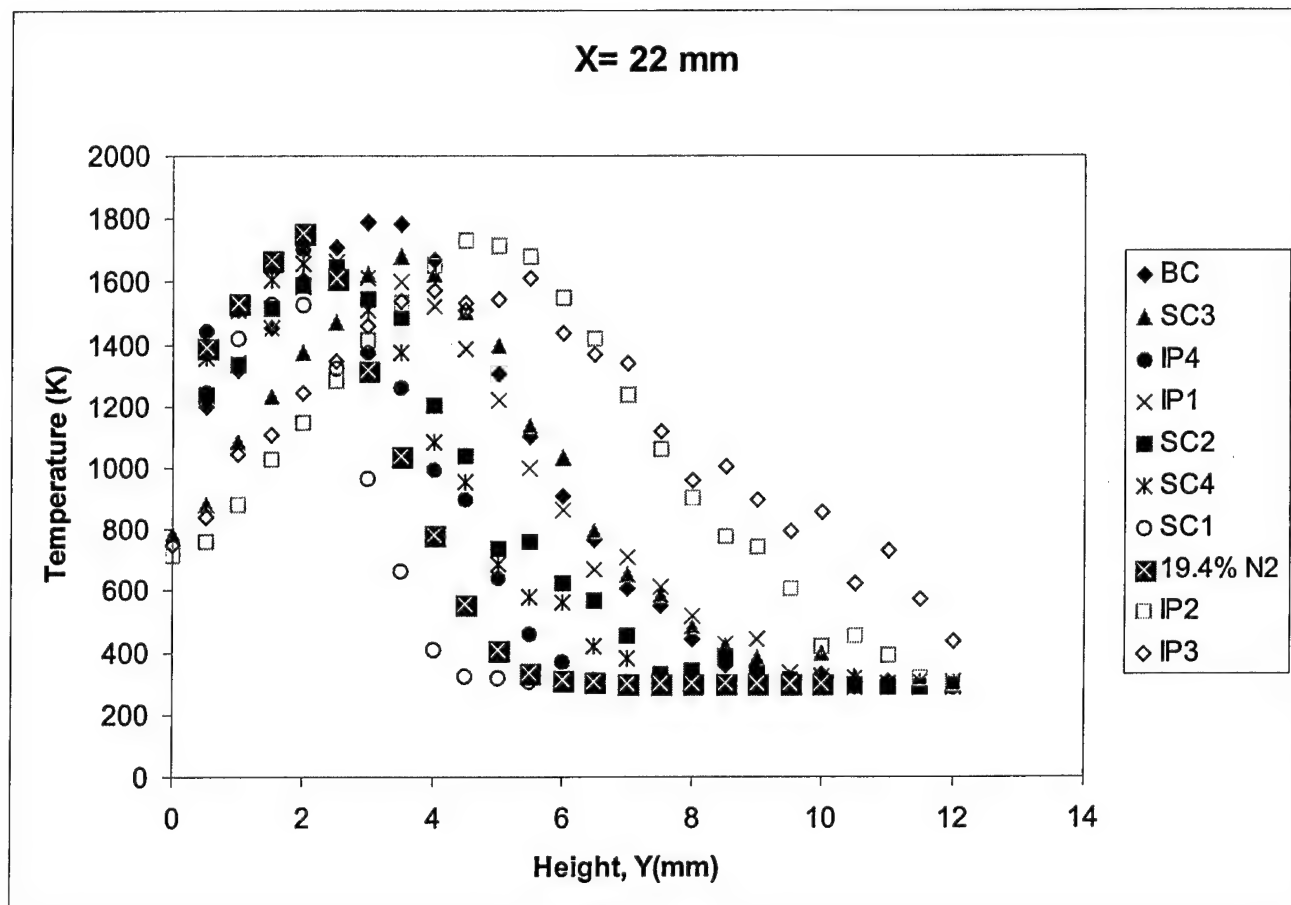Figure 7: Picture of flame with mist from nozzle, showing turbulence and quench zone in the leading section

Figure 8: Comparison of temperature profiles between base case nozzle mist case
with high flow disturbance

21

Figure 9: Temperature profiles in tests without mist and tests with pressure atomizing nozzles $U_\infty = 84$ cm/s

induced turbulence. In the nitrogen test, additional nitrogen was added to the air in the plenum (Fig. 1) to get the oxygen concentration to 19.4%. Details about this test are in Reference 22. In most of the mist tests the temperature seems to be enhanced slightly on the fuel side of the diffusion flame. The exceptions are the tests with SC3 and IP2 and IP3, which show some suppression. On the other hand, the flame temperature was suppressed on the airside of the flame (right side of the peak) by the addition of mist or nitrogen. The reduction of temperature on the airside seems to suggest that droplet evaporation is mainly outside the flame. However a closer look reveals that the test with largest droplet diameters (SC1) seem to give the highest suppression, contrary to what one would expect.

However we will keep in mind that in the nitrogen and mist tests, a quench zone is established near the leading edge when the sample is moved to the measurement location. In some cases the quench zone is ~ 20 mm. Since the boundary layer flame is anchored further downstream than $X = 0$ the thermal boundary layer is expected to be much thinner at the thermocouple location in the tests with quench distance than the one without (base case). Thus the thermocouple would have to come much closer to the surface in the mist cases to measure high temperatures. Therefore the apparent temperature reduction on the airside at this X location may be due mainly to the establishment of the quench zone in the leading section. The shift in flame anchor location is expected to influence the value of the flame standoff distance (Y at temperature peak) δ. In the mist and N_2 tests the flame was anchored closer to $X = 22$ mm than the base case. Therefore, the δ's in these tests are expected to be smaller since in boundary layer flames δ goes as square root of the distance from flame anchor location. Figure 9 shows this. For example in Fig. 9, $\delta = 3$, 2.0 2.5 and 2 mm for the base case, SC1, SC2 and N_2 cases, respectively. The temperature profiles with IP2 and IP3 seem to show a different trend from the rest of the pressure atomizing nozzles. Figure 9 shows that the flame standoff distances in tests with these nozzles are higher than that with the base case. At $X = 22$, δ is ~4.5 mm for the IP1 and IP2 tests compared to ~3 mm for the base case. Both nozzles produced much smaller droplets than the rest of the pressure atomizing nozzles, about 4 times less than SC1, for example.

Figure 10 shows the temperature profiles at $X = 37$ mm from the upstream edge. The trend is similar to what is shown in Fig. 9 except that the enhancement in temperature in the fuel side of the flame is larger with the nozzles except for SC3 and IP2 and IP3. Temperature is also reduced on the airside of the flame. The δ is smaller with mist than without mist and the difference is slightly larger at $X = 37$ mm than at $X = 22$ mm. For example, in Fig. 10, δ ~ 5.5, 4.0, 4.5 and 4.5 mm for the base case, SC1, SC2 and nitrogen cases, respectively.

Figure 11 shows the temperature profiles at $X = 57$ mm from the upstream edge. It shows similar trends as was shown in Fig. 10; namely that gas phase temperature is reduced on the air side of the flame and enhanced on the fuel side. The enhancement is now larger than in Figs. 9 and 10 and fuel side temperature was enhanced in all the tests.

23
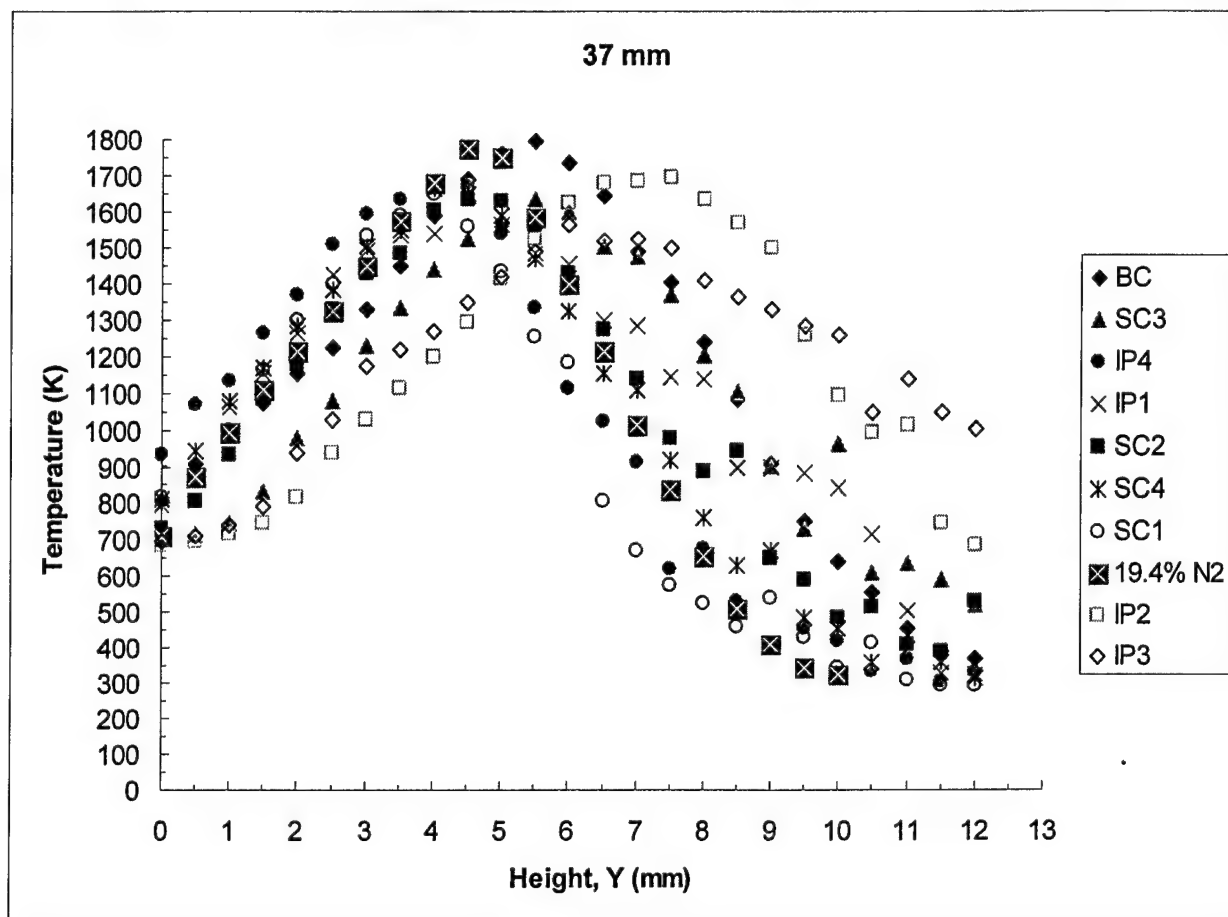
Figure 10: Temperature profiles in tests without mist and tests with pressure atomizing nozzles $U_\infty = 84$ cm/s
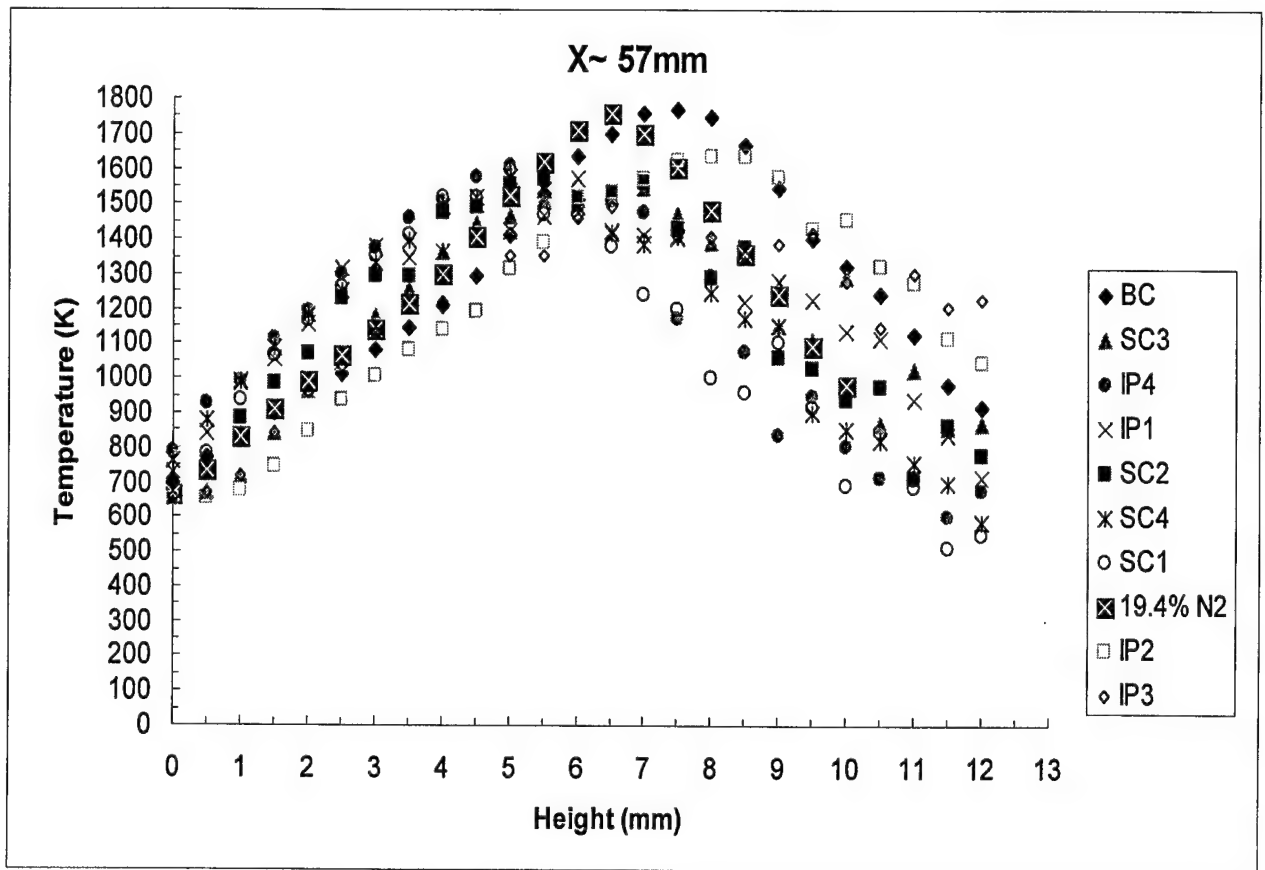
Figure 11: Temperature profiles in tests without mist and tests with pressure atomizing nozzles U$_\infty$ = 84 cm/s

At $Y = 3$ the lowest temperature (base case) was ~ 850 K while the highest temperature was ~ 1350 K (IP1) The reduction in temperature on the airside is also very significant. The flame stand off distance δ is also smaller with mist than without mist at this location. It is ~ 8, 5, 6 and 6.5 mm for base case SC1, SC2 and N_2, respectively. Once more the difference in δ and the enhancement in temperature on the fuel side is progressively increasing. The peak temperatures with mist, especially with solid cone nozzles were suppressed by about 200 K.

Figure 12 shows the temperature profiles for $X = 78$ mm. The profiles show similar trend as Figs. 9-11. The trend is now more defined than was the case in the earlier figures. The flame standoff distance is suppressed the most in Fig. 12 than in Figs. 9-11. For example δ is ~ 9.5, 4, 5.5 and 9 mm for base case, SC1, SC2 and N_2 respective. At $X = 78$ mm the effects of flame attachment location on δ is expected to be less significant since δ goes as $X^{0.5}$. Hence there is very little difference between the values of δ downstream in N_2 and base case tests. Therefore the suppression in flame stand off distance is due to other effects of nozzle mist other than flame anchor location. The peak temperature is also reduced in Fig. 12 by the cooling effects of mist. For example the peak temperature at $X = 78$ mm in the base case is about 1650 K but with SC1, it is about 1450 K. Figure 12 also shows (qualitatively) that the temperature gradient near the surface ($X = 0$) is higher in tests with mist than in the base case and nitrogen tests. This implies that the heat feedback to the sample surface, which is proportional to the temperature gradient increases with addition of mist from the pressure atomizing nozzles. A closer look at the profiles in Figs. 9-12 reveals that the effects of mist from the nozzles (lower δ, higher temperature and temperature gradient near the surface) seem to progressively increase as X increases. Since these trends were obtained in the tests with pressure atomizing nozzles where, the flames were turbulent (Fig. 7) and not in the tests with NanoMist, where the flames were laminar (Fig. 4) one would suspect that mist-induced turbulence played a significant role in the observed trends. It seems therefore, that the effect of the mist-induced disturbance in the flame brings the flame closer to the surface on the average. As the flame comes closer to the surface, the heat feedback to the solid significantly increases. In summary the effects of mist outlined above strongly suggest the following (a) that in the downstream section ($X>37$ mm) the heat feed back to the PMMA surface increased when mist was introduced with nozzles and (b) that the enhancement in heat feedback increased with X. This is consistent with the expectation that the effects of induced turbulence increases with Re_x as will be shown later.

The effects of nozzle-induced flame fluctuation on flame standoff distance δ is shown more clearly in the plot of δ/X versus $Re_x^{-0.5}$ (Fig. 13). Using the properties of PMMA and the temperatures measured in base case boundary layer flame, the Emmons's [25] steady state expression for δ/X is given as
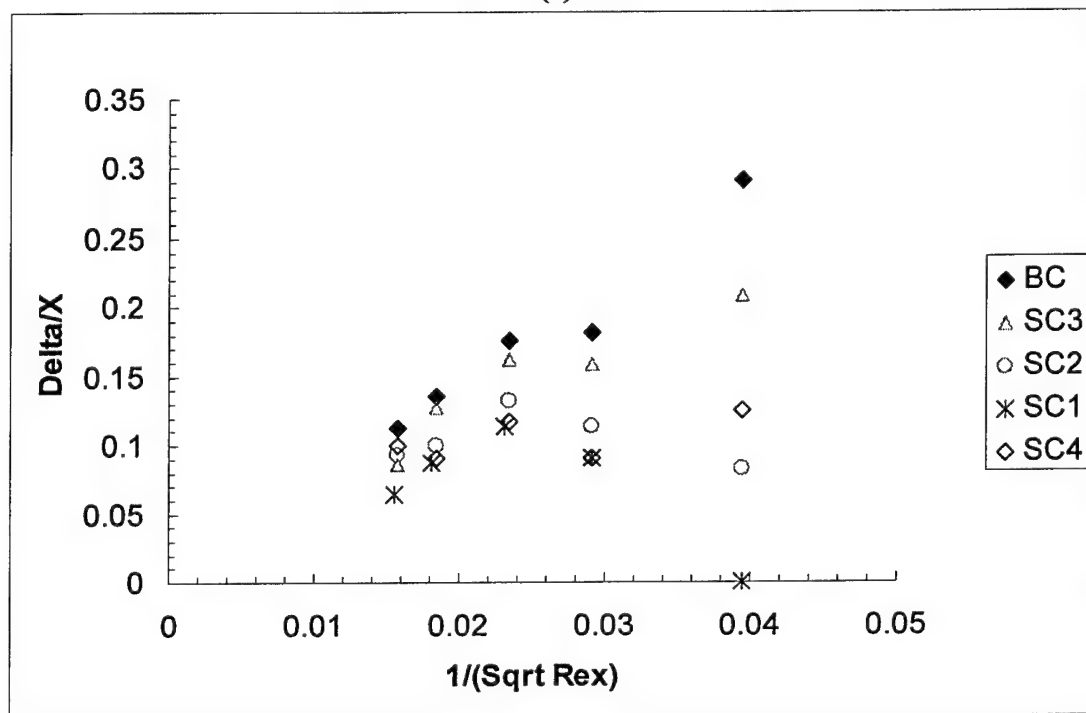
$$\delta/X = 10Re_x^{-0.5}. \tag{1}$$

Details about equation (1) are given in [14,15]. Since this equation is derived from boundary layer analysis, it is not valid near the leading edge. Hence δ/X is linear with
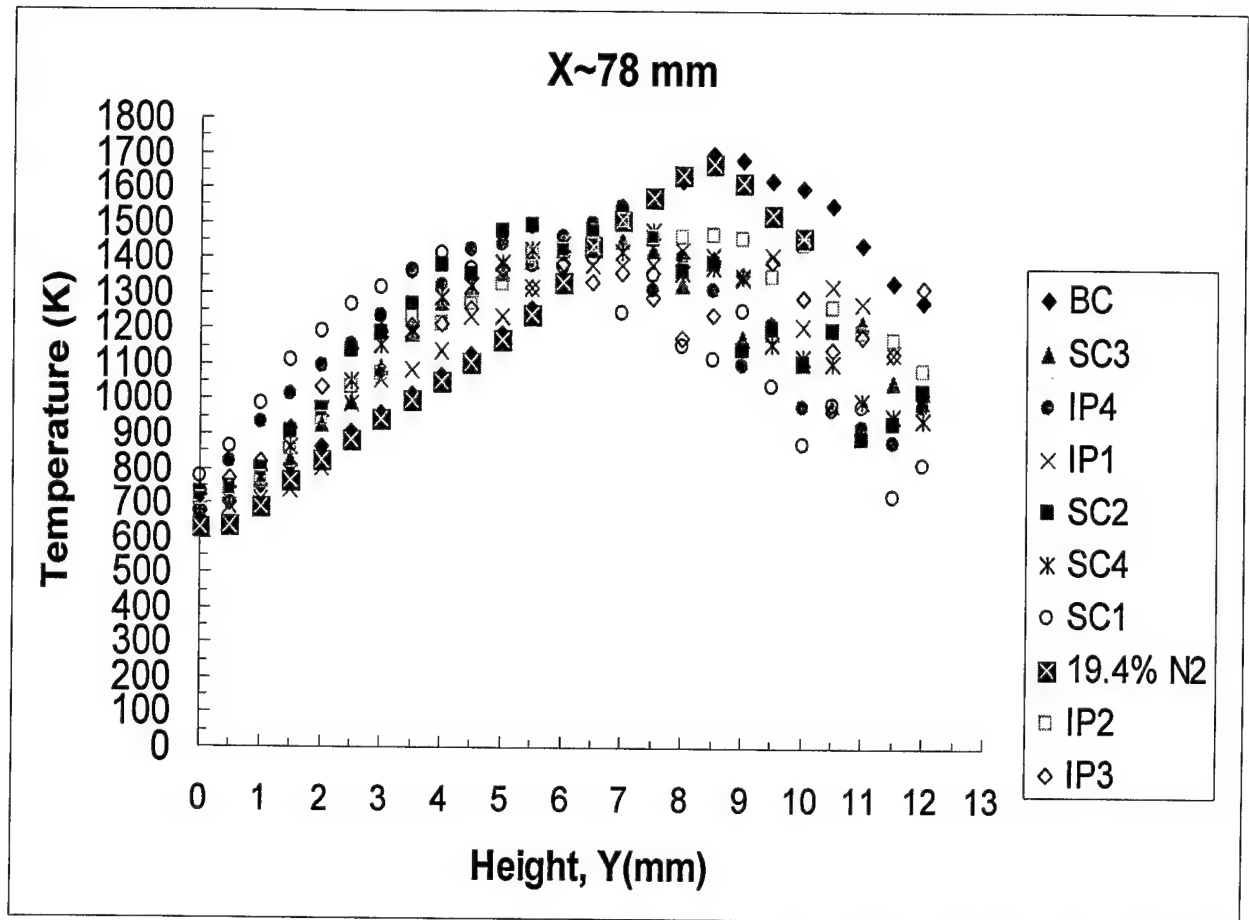
Figure 12: Temperature profiles in tests without mist and tests with pressure atomizing nozzles $U_\infty = 84$ cm/s
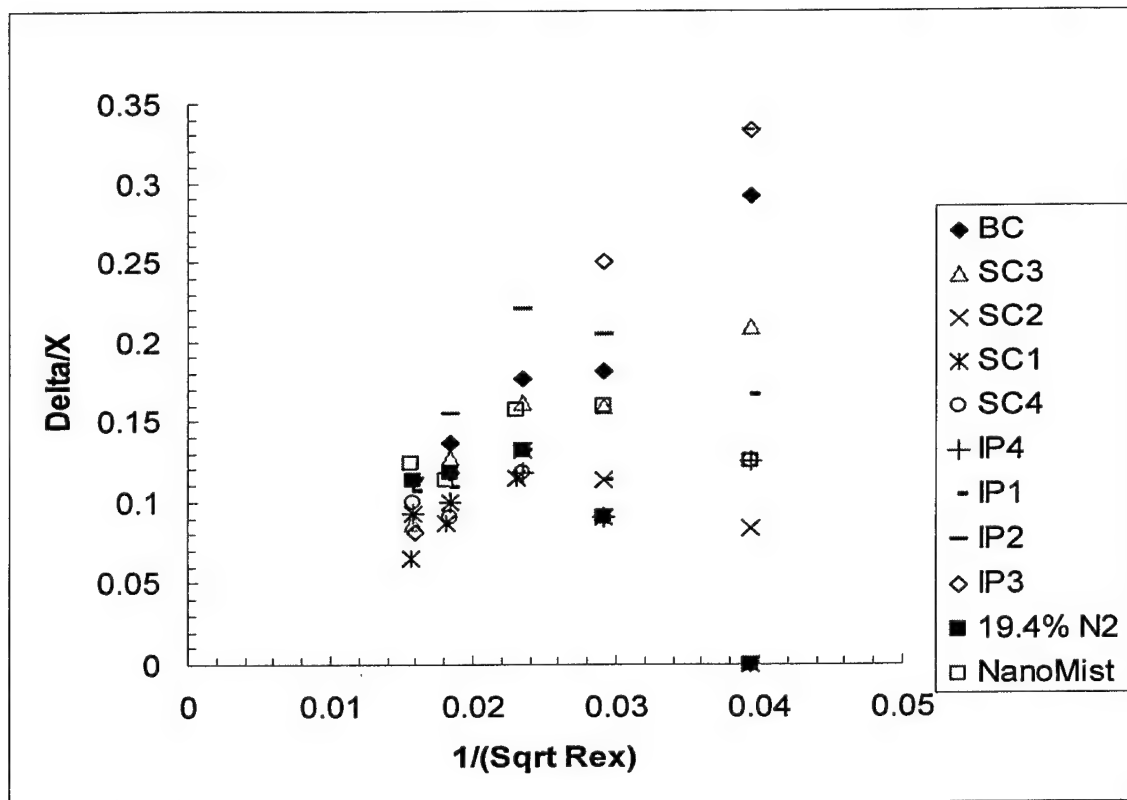
(a)

(b)

Figure 13: Variation of flame standoff distance with stream-wise location in tests with (a) all pressure atomizing nozzles (b) solid cone nozzles

$Re_x^{-0.5}$ for the base case far from the upstream edge as Fig. 13 shows. $Re_x^{-0.5} \sim 0.04$ (X ~ 12 mm) could be said to be far from the upstream edge, where the base case flame is anchored. Also included in Fig.13 are data from N_2 and NanoMist (4.3% mass loading) tests. As expected, the PAN mist data are below the base case data everywhere. However, the data from two impingement pin nozzles IP2and IP3 deviate from this trend. The N_2 and Nanomist data are very close to the base case for small $Re_x^{-0.5}$, corresponding to the trailing section and are smaller than the base case for large $Re_x^{-0.5}$ (leading section). This is consistent with what is shown in Figs. 9-12 above. The mist data seem to show a linear trend like the base case in the trailing section up to about $Re_x^{-0.5} \sim 0.025$ but deviate significantly from this trend upstream. Because of the upstream shift in the flame anchor location in the mist and N_2 tests, the measurement locations $Re_x^{-0.5} \sim 0.04$ (X = 12 mm) and $Re_x^{-0.5} \sim 0.03$ (X = 22 mm) are no longer far from the leading edge of the flame. Hence, the boundary layer linear relations could no longer hold. Indeed, at $Re_x^{-0.5} \sim 0.04$ (X = 12 mm) δ is zero for the N_2 and SC1 tests because the flame was downstream of the location since of the quenching distance ≥ 20 mm. Figure 13 shows clearly that the decrease in δ downstream in the mist tests is due to the effects of turbulence, but the decrease in δ upstream is due to the upstream shift in flame anchor location. Figure 13b shows these effects more clearly for solid cone nozzles.

The spray-induced disturbance, which causes the turbulence observed in the downstream section of the flame, could be related to the mist incoming momentum density M, at the point of injection. M can be estimated as

$$M = N_d\, d_d^3 \rho_w Q4/(6d_o^2), \qquad (2)$$

where N_d = droplet number density
$\quad d_d$ = droplet volume mean diameter
$\quad \rho_w$ = density of water
$\quad Q$ = measured total nozzle flow rate at the test pressure
$\quad d_o$ = nozzle orifice diameter.

The droplet number density and mean volume diameter are obtained from data measured with Malvern Spraytec$^{©}$ at the exit of the tunnel. We realize that these values could be different between the point of injection and the tunnel exit because of losses at the tunnel walls. However, the error introduced by using values measured at the tunnel exit are not expected to substantially change the relative effects of mist injection when the same type of nozzles are compared. The solid cone nozzles for example are of the same make and have the same spray angle (60°). Thus the estimated momentum densities could be used to approximate the disturbance due to each nozzle injection for comparative purposes. The estimated momentum densities from the various nozzles at the test conditions are listed in Table 3. Unlike the solid cone nozzles the effective disturbance caused by the impingement pin nozzles may not be well estimated with the above expression, since the flow exiting the nozzle orifice impinges on the pin in front of it where its impact is reduced. The effect of this stagnation flow is not taken into account in the above estimate. However the numbers in Table 3 may be useful for comparisons between the

29

impingement nozzles. A dimensionless Reynolds number, Re_m can be defined in terms of the droplet momentum density as

$$Re_m = MX/\mu_\infty, \tag{3}$$

where μ_∞ is the viscosity of the ambient air.

Table 3: Estimated droplet momentum densities in tests with the pressure atomizing nozzles

Nozzle Identification	Droplet momentum density at nozzle exit $(g/cm^2 \ s)$
SC1	3.21
SC2	3.29
SC3	2.61
SC4	2.46
IP1	29.17
IP2	25.95
IP3	48.81
IP4	8.07

To relate the Re_m to the induced fluctuations in the flame, we define a dimensionless temperature θ obtained from the temperature-time measurements at various points in the flame (Fig. 3). At a given X and Y the 100-temperature data set was averaged to obtain a T_{ave} and a standard deviation T_σ was calculated. A dimensionless temperature is obtained as T_σ / T_{ave}. θ could represent a qualitative measure of flow disturbance in the flame.

Figure 14 is a plot of Re_m versus θ for tests with solid cone nozzles for temperatures in the leading and middle sections of the flame X = 22 and 37 mm and Y = 4 mm. At these X locations the thermal boundary layer thickness is thin and the Y location is on the airside of the flame at X = 22 mm but at the flame (peak temperature) location at X=37mm. Figure 14 also includes the base case datum, where the Re_m = 0, since there is no induced disturbance in the wind tunnel in this case. Written next to the data points are the calculated momentum densities in these tests. Figure 14 shows that at X=22 mm, there is no correlation between Re_m and θ. For example, the effects of flow fluctuations seem to be higher in tests with lower mist momentum densities compared to those with higher momentum densities. Figure 14 on the other hand show that at X= 37 mm there is some correlation between Re_m and θ and that higher mist momentum gives rise to higher flow fluctuations.
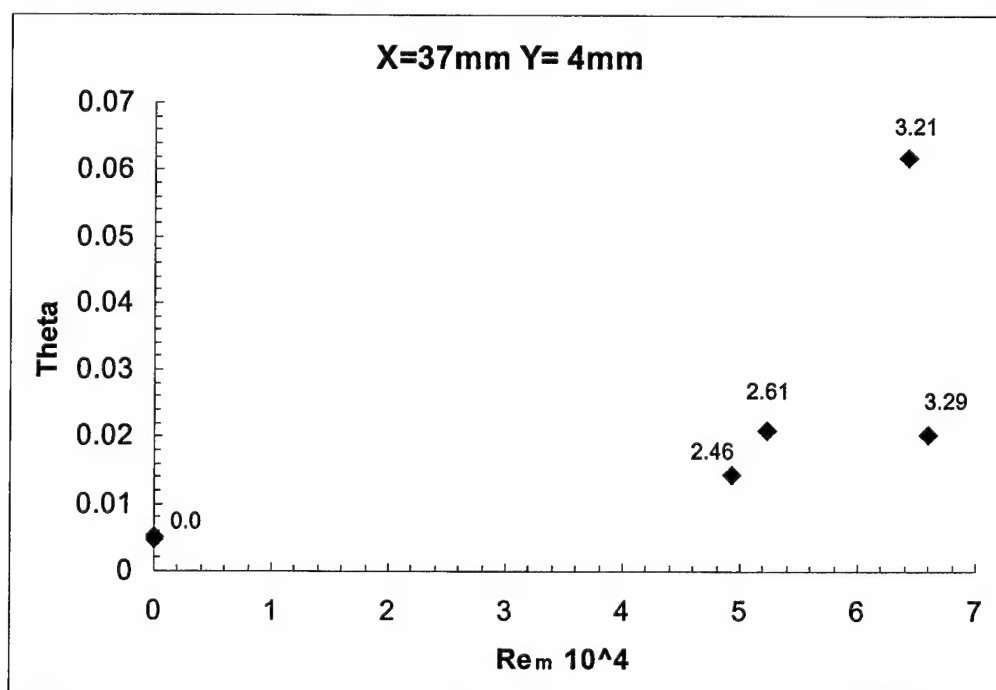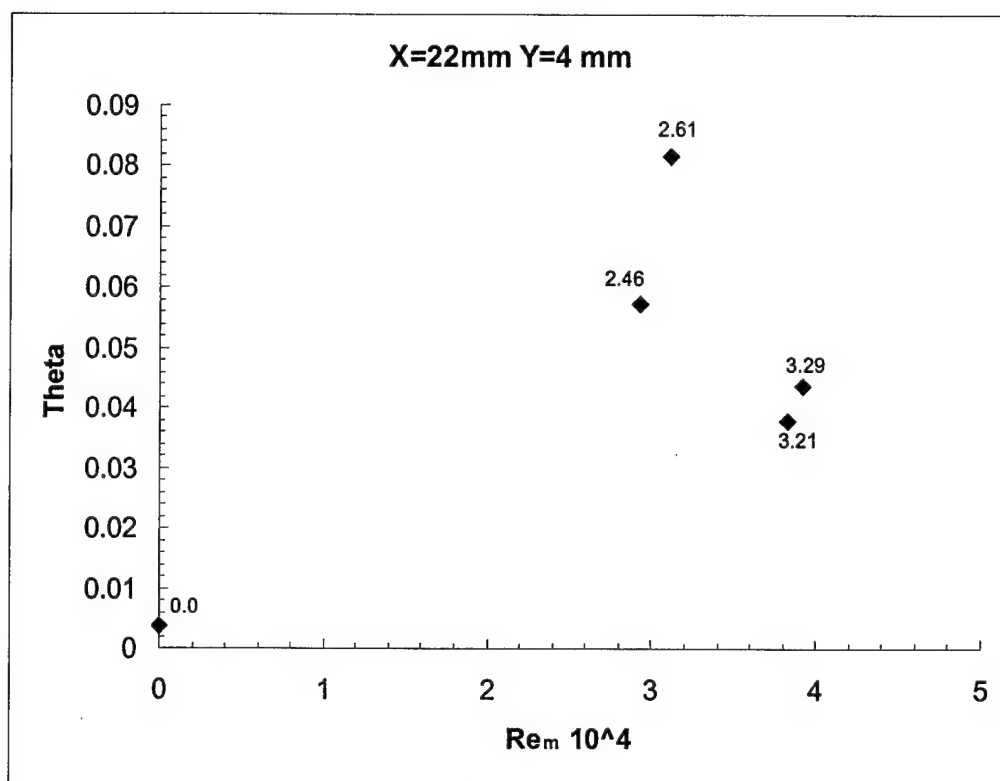
Figure 14: Relation between temperature fluctuation and droplet momentum density at two points in the flame

Figure 15 shows similar plots at X = 57 and 78 mm and Y = 8 and 12 mm. These points are on the airside of the boundary layer flame where flow instability is expected to be highest [24]. Figure 15 shows that θ increases with Re_m, indicating that the disturbance induced by nozzle action in the tunnel correlates with flow fluctuations in the downstream section of the flame. For example, at X = 78 mm a comparison of the tests with momentum density of 0.0 (base case) and that with momentum density of 3.21 g/cm^2s (SC1) show that θ increased by about 6 times at Y = 12 mm and about 3 times at Y = 8 mm. Y = 12 mm is on the airside of the flame and Y = 8 is about the peak temperature location for X = 78 mm. This is consistent with the observations of Ahmad and Feath [24] that turbulence begins at the outer edge of the boundary layer and propagates towards the solid surface. At X = 57 mm and at the 2 heights θ increases with Re_m and higher momentum densities give rise to higher temperature fluctuations. Finally, one can deduce from Figs. 14 and 15 that Re_m correlates better with θ downstream than upstream. Indeed, the correlation gets better as X increases. Thus, turbulence induced by mist spray action in the wind tunnel is propagated down stream and causes flame fluctuation which is most significant in the trailing section of the flame (higher Re_x). This is consistent with the results of Ahmad and Faeth [24]. In natural convection fire experiments, they observed that transition from laminar to turbulent flow occurred at high Grashof numbers Gr_x, which is the Re_x equivalent in natural convection.

The results of the effects of PAN mist on flame temperature can be summarized as follows:

(1) Mist induced turbulence makes the flame fluctuate and the fluctuation is not significant near the upstream edge. However, it is very significant downstream and the turbulence increases with stream-wise location.

(2) The effects of the turbulence is such that heat feed back to the solid surface increases. This is because the flame is brought closer to the surface and the temperature and temperature gradient on the fuel side of the flame is increased. These effects increase with X downstream. These results imply that mist-induced turbulence in the tests with nozzles would strongly affect the local burning rate downstream as we shall show later.

3.3 Effects of Mist on Local Burning Rate

Detailed discussion of the burning characteristics of the PMMA plate under a laminar boundary layer flame without mist are given in our earlier papers [14,15] There it was reported that the local burning rate of the plate varies with X and time. It is well known that the burning rate is highest near the leading edge where heat feedback is highest and decreases sharply with X. Figure 16 is a picture of the cross section of the PMMA after 5, 10 and 20- minute tests without mist. The tests were run at U_∞ = 84 cm/s. One notes from Fig. 16 that the burned thickness is much larger upstream than downstream and also larger in 20-minute test than in the 5-minute test. Therefore, one would expect the error in the burning rate measurement to be highest downstream at short times. In the leading section and/or at high velocities, where convection heat transfer rates
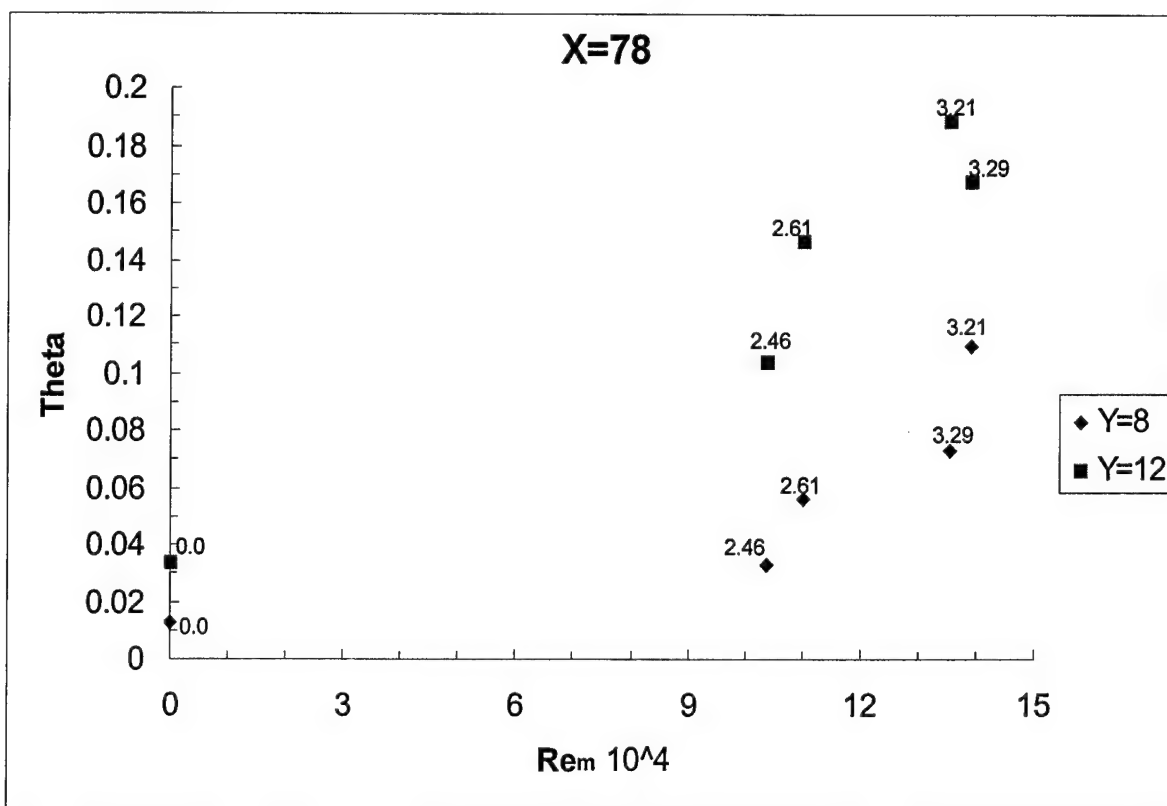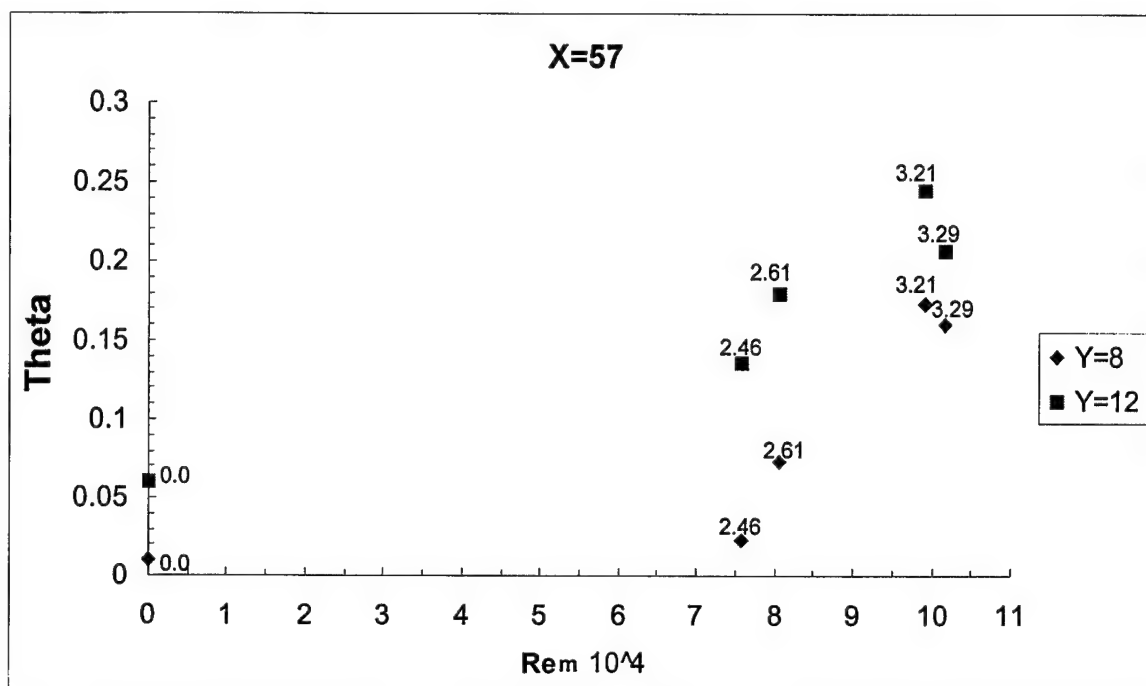
Figure 15: Relation between temperature fluctuation and droplet momentum density (Re_m) at four points in the flame
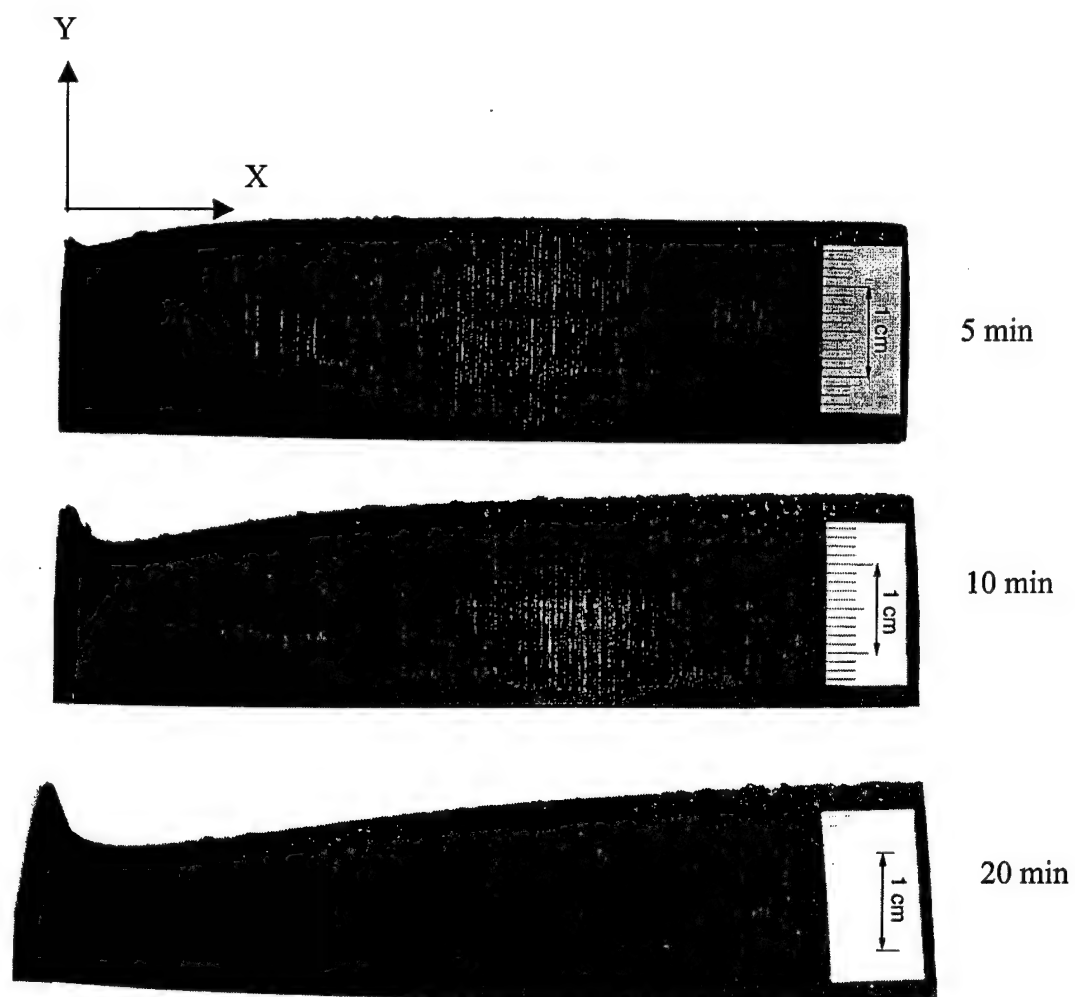
Figure 16: Pictures of PMMA sample surface profiles after 5, 10 and 20-minute burn, $U_\infty = 84$ cm/s

are high, the error is smaller. For example, for U_∞ = 84 cm/s and X = 5 mm the error in the measured time-averaged regression rate is approximately 8% (5 min). Downstream at X = 70 mm with U_∞ = 84 cm/s, it is approximately 30% (5 min).

Also in [14,15] we showed that the local burning rate varies with time as well. It decreases with time in the leading section due to moving boundary effects and it increases with time downstream due to transient heat conduction into the solid. In the following sections we present the effects of NanoMist and that of mist from pressure atomizing nozzles on the burning rate of the PMMA plate. It is expected that the effects of mist on burning rate in the two systems would be different just like we saw with flame temperature profiles in the previous section.

3.3.1 Effects NanoMist on Local Burning rate

Figure 17 shows the local burning rate as a function of X in a 10-minute base case and NanoMist tests with U_∞ of 84 cm/s. The base case test is one with a cross flow but without mist. To achieve cross flow without mist the mist extracting fan is turned on to blow air through the generator (see insert in Fig.1) but the piezoelectric discs are not energized and mist is not generated. A comparison of these two cases will reveal the effects of just the mist droplets and accompanying water vapor. Results of two NanoMist (+vapor) mass loadings of 4.3% and 2.5% are shown in Fig.17. Figure 17 shows that time-averaged burning rate increases sharply near the upstream edge, reaches a peak and decreases sharply downstream. The regression rate is suppressed very significantly by Nanomist in the leading 10 mm of the plate. For example at X = 5 mm the regression rates are 0.56, 0.42 and 0.22 mm/min for the base case, 2.5% NanoMist and 4.3% NanoMist respectively. The peak burning rate is suppressed with mist but not significantly. For example it is ~ 0.58 mm/min in the base case and about 0.54 m/min in the test with 4.3% NanoMist. However, the location of the peak regression rate shifted slightly downstream with the addition of mist. It shifted by about 5 mm when 4.3% Nanomist was introduced. This is due to the establishment of a small quench zone when mist was introduced. Between the peak location and X ~ 30 mm the mist suppression in burning rate is very small. At X = 20 mm for example it is negligible but increases with X further downstream. At X = 50 mm the regression rates are ~ 2.2, 1.6 and 1.4 mm/min for base case, 2.5% Nanomist and 4.3% NanoMist, respectively. Thus the suppression in burning rate is higher in the leading section than downstream. This is consistent with the temperature results in Figs. 5 and 6, where we saw that NanoMist suppression of flame temperature is more in the leading section than downstream. The ultra fine mist droplets evaporate quickly resulting in local gas phase cooling. It follows that the surface regression rate, which is dependent on the rate of heat feedback from the flame would follow the same trend as the gas phase temperatures.

The effects of varying the mist loading are shown in Fig. 17. It was not possible to vary the mass loading through a wider range at 84 cm/s because the window is narrow. The flame blows off at mass loading higher than 4.3% and very little suppression is obtained with mass loading less than 2.5%. Furthermore Fig. 17 shows that the difference
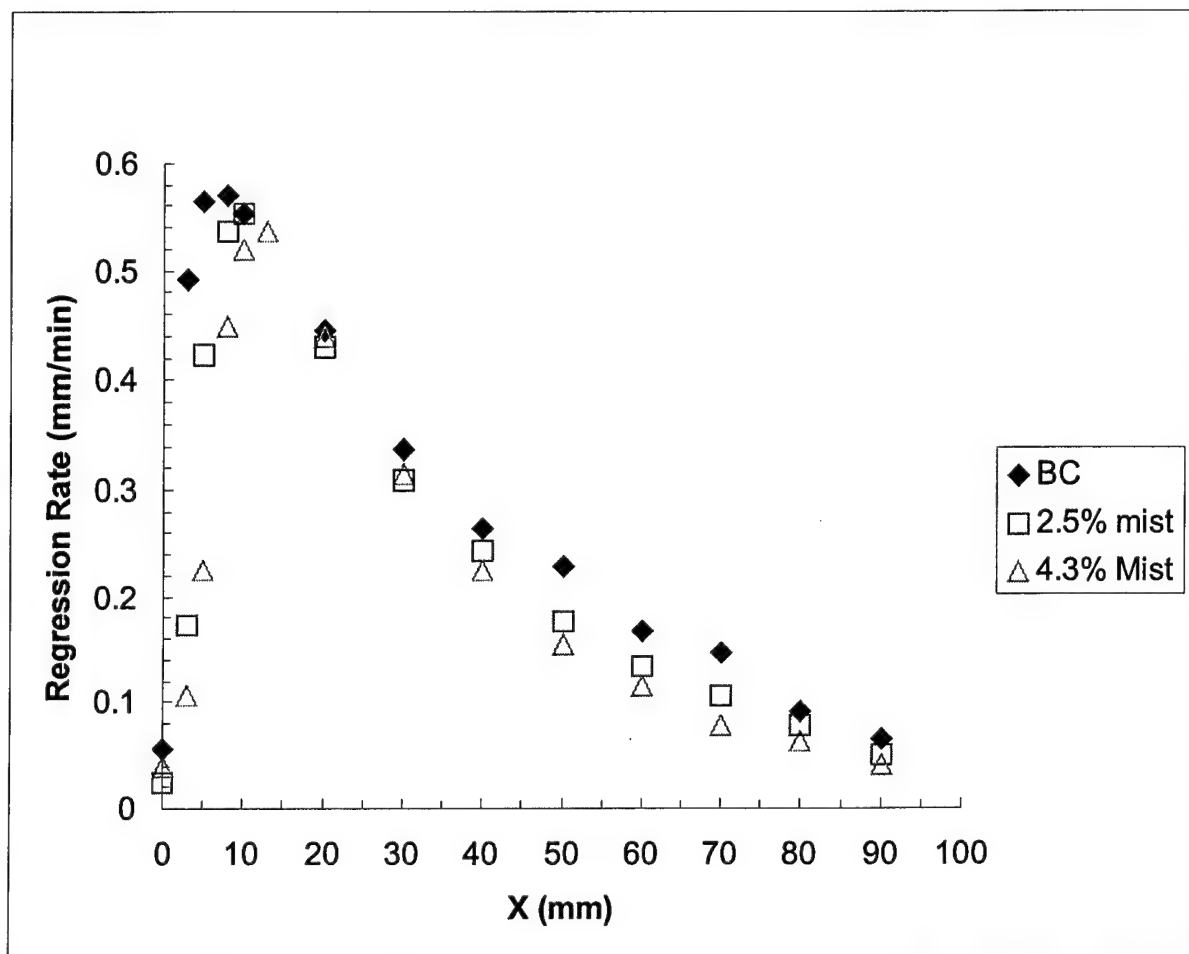
Figure 17: Effects of NanoMist on surface regression rate at various stream-wise location, X. $U_\infty = 84$ cm/s

between the 4.3% data and 2.5% data is not much. At every location along the PMMA surface, the suppression in regression rate increases with mist mass loading. The difference between the results with 2.5% and 4.3% tests is very small downstream, unlike upstream. The blow off concentration is a strong function of inlet velocity. At high inlet velocities one needs very little mass loading to blow the flame off. It could be because a combination of high velocity (short flow time) and mist cooling effects (long reaction time) reduces the local Da and so the flame becomes unstable and blows off. For example, we ran some tests with U_∞ of 120 cm/s and found out that we could not obtain a stable flame for mist mass loading greater than 1.8%. At this mass loading the cooling effects were small and suppression in burning rate was negligible.

It is well known that the heat feedback to the solid in a boundary layer combustion is very small in the trailing section compared to upstream. We showed in [14,15] that the burning rate of the PMMA plate without mist in the trailing section increases with time because it takes the solid considerable time to warm-up and start pyrolyzing at a steady rate because of the slow heat transfer rate and in-depth heat conduction. On the other hand, in the leading section where the heat feedback rate is very high, the surface warms up quickly and regresses rapidly, creating a valley, which deepens with time. As the valley deepens the heat feedback to the curved surface reduces and the regression rate decreases. Next, we present results in tests without mist and with 4.3% NanoMist, which lasted 5, 10 and 20 minutes to reveal the effects of the mist cooling on the transient processes in the burning PMMA plate. The transient effects are seen more clearly in terms of the dimensionless burning rate (Nusselt number) Nu_x, where Nu_x is given [14,15] by

$$Nu_x = R\rho_s LX/(\lambda \Delta T); \tag{4}$$

where R is the local regression rate, ρ_s is the density of air, L is heat of pyrolysis of PMMA (1.6KJ/gm [26]), X is the stream-wise distance from the PMMA leading edge, λ is the thermal conductivity of air and ΔT is the temperature difference between the pyrolyzing surface and the "flame location". This is estimated as ~1200 K since the peak temperature in the flame is ~ 1800 K and molten surface temperature is ~ 600 K [15,27]. Emmons's steady state equation for boundary layer burning rate of the PMMA plate is obtained as [14,27,28]

$$Nu_x = 0.1\, Re_x^{0.5} \tag{5}$$

Figure 18 shows a plot of Nu_x versus $Re_x^{0.5}$, which compares base case with NanoMist results at U_∞ of 84 cm/s. The solid symbols are for the tests without mist while the open symbols are the data with Nanomist. The Emmons's steady state linear relation is shown as a straight line in Fig. 18. It helps to reveal (qualitatively) the deviation from steady state.

At low $Re_x^{0.5}$ (the leading section), the burning rate decreases with time in the tests with and without mist as a result of the moving boundary effects outlined earlier. For

37

example, for $Re_x^{0.5}$ ~16 (X~5 mm), Nu_x is ~2.1, 1.4 and 0.98 for the base case in 5, 10 and 20 minutes, respectively, but it is ~ 1.7, 0.57, and 0.45 for the mist tests at those times, respectively. Figure 18 shows that the burning rate with NanoMist is less than that without mist at any given time because of cooling.

In Fig. 18, for high values of $Re_x^{0.5}$ (the trailing section) the burning rate increases with time in both the tests with and without mist. For example, at $Re_x^{0.5}$ = 70 base case Nu_x is ~ 1.75, ~2.75 and ~6 in 5, 10 and 20 minute tests, respectively. At the same location in tests with mist Nu_x is ~0.75, 1.75 and 3 in 5, 10 and 20 minute tests, respectively. Again the cooling effects of mist give rise to the lower rates (heat feed back and burning) in the mist tests. Ananth et al [14,28] reported a steady state numerical solution of Navier Stokes equations for the boundary layer burning of the PMMA plate without mist. Their results compare well with experimental data at long times and both reveal that steady state is attained later as X increases. Since the heat feedback rate to the surface in this section is much less in the mist case than in the base case, because of the gas phase cooling, the PMMA plate would take longer time to warm up and start pyrolyzing vigorous in the tests with NanoMist. Therefore steady state is attained later in the mist case than in the base case. For example in 20 minutes the base case seem to be approaching steady state downstream up to about $Re_x^{0.5}$ ~ 60, since the data fall approximately along a straight line. Thus, steady state seems to have been approached in 20 minutes up to ~70 mm downstream in the base case. In the mist case on the other hand, burning rate seems to be approaching steady state in 20 minutes up to $Re_x^{0.5}$ ~50 (X = 50 mm).

The effects of Nanomist on the transient burning rate downstream is made clearer in a plot of dimensionless burning rate Nu_x versus dimensionless time Fo shown in Fig. 19.

$$Fo = \alpha t/(\Delta y)^2 , \qquad\qquad (6)$$

where α is the thermal diffusion coefficient for PMMA (1.0776×10^{-3} cm^2/s), t is the burn time and Δy is the PMMA plate thickness (2.3 cm). Figure 19 shows data at X= 90 mm for the base case and for NanoMist with 4.3% mass loading and U_∞ = 84 cm/s. The solid line is for the base case while the dashed line is for the mist. By considering the slopes of the two lines, one can deduce that the burning rate is increasing faster (larger slope) without mist than with NanoMist. Thus the cooling effects of NanoMist downstream means that the PMMA plate warms-up more slowly and thus the burning rate would take longer time to reach steady state.

Finally, in the NanoMist experiments the droplets are very tinny (~3 μm) and they follow the streamlines. They are unlikely to penetrate far into the flame before they evaporate and if they do, it is unlikely that some droplets would survive in the flame and reach the fuel surface. Therefore direct PMMA surface cooling by these droplets is highly unlikely. Hence, the suppression in burning rate measured in these tests with NanoMist is
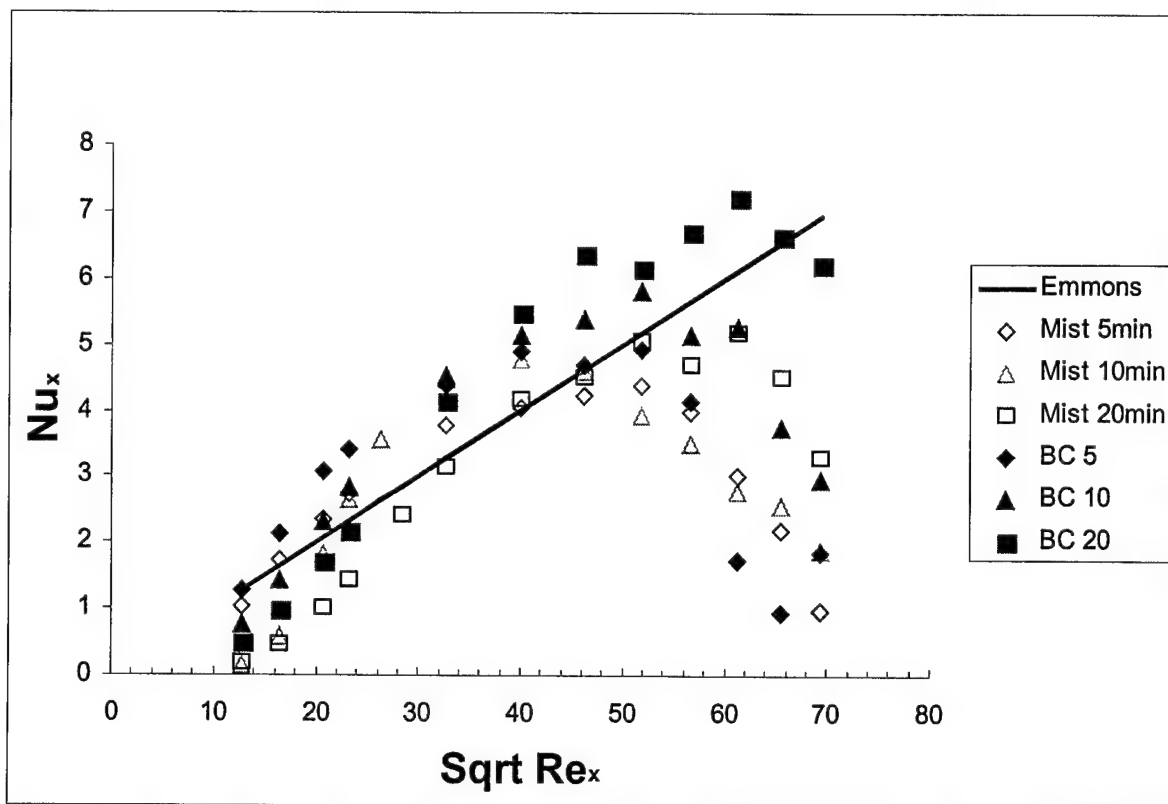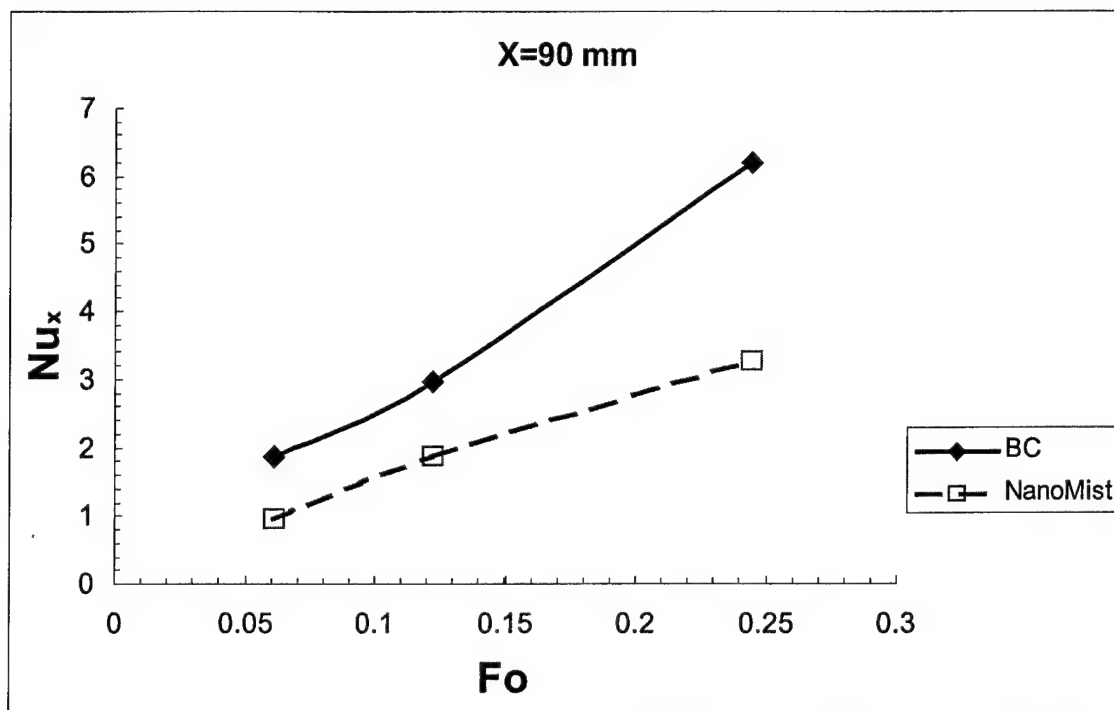
Figure 18: Normalized burning rate Nu$_x$ versus Re$_x^{0.5}$ in 5, 10 and 20-minute tests with 4.3% NanoMist and base case U$_\infty$ = 84 cm/s

Figure 19: Normalized burning rate Nu_x versus dimensionless time Fo in tests with 4.3% NanoMist and base case $U_\infty = 84$ cm/s

mainly due to the cooling of the gas phase by extraction of heat of vaporization and vapor specific heat and also by water vapor dilution of oxygen concentration.

3.3.2 Effects of Mist from Pressure Atomizing Nozzles (PAN) on the Local Burning Rate.

The spray nozzles and the airflow are turned on before the flame is ignited under a radiant panel, which is 40 cm downstream from the tunnel exit. This ensures that the mist flows at a steady rate throughout the test duration. At ignition the flame is anchored at the sample leading edge. The burning PMMA plate is then moved to the tunnel exit, where the velocity of the mist-laden air is higher. If the mist flow rate is very high, the flame is dislodged at the PMMA leading edge and eventually blown off. In this case the Da is too low within the measurement location and the flame could not sustain. Thus flame extinguishment under these conditions is obtained by the creation of instability, dislodging the leading edge and eventual blow-off. Fig. 20a shows a picture of a flame being blown off. It is interesting to note that the PMMA surface is still flat as the flame is being blown off. At lower mist flow rate, the flame only retreats from the leading edge and stabilizes downstream, establishing a quench zone, where the Da is too low for stability (Fig. 20b). As the surface curvature changes near the flame front, the flame creeps slowly upstream, decreasing the quench zone with time. In an earlier paper [22] we showed that this unexpected flame spread is caused by the non-uniform surface regression, which is characteristic of the boundary layer combustion of PMMA. In some tests the flame could not spread up to the leading edge during the 10 minutes of the experiment. Figure 21 shows the surface profiles of three 10-minute tests. Figure 21a is the profile for the base case test, where the flame was anchored at the sample leading edge throughout the 10 minutes, while Figs. 21b and 21c are the profiles for tests with IP1. and SC3. In the last two cases, the flame had not spread up to the leading edge within the 10 minutes. The surface profiles show the usual high regression in the leading section, which decreases with X.

The time-averaged surface regression rates at various stream-wise locations for tests with nozzles and the base case are shown in Fig. 22 All the tests lasted 10 minutes and inlet velocity was 84 cm/s. There were tests with 4 solid cone (SC) nozzles and 4 impingement pin (IP) nozzles. In theses tests a change in pressure or orifice size changes both the mist flow rate and droplet size. Thus, mist mass loading could not be changed independent of the droplet size. Thus the tests with various nozzles show the combined effects of droplet size and mist mass loading. The various tests are identified in Fig. 22 and the details of nozzle and mist parameters were given in Tables 1 and 2.

The solid diamonds in Fig. 22 represent the base data. As expected, the burning rates increase sharply with X near the leading edge, reach a peak and then decrease with X downstream. For X <20 mm the burning rates with mist are less than the burning rates without mist except for tests with IP2 and IP3 where the burning rates are higher than the base case for 3 <X <10 mm. The time-averaged peak regression rates with mist (excluding IP2 and IP3) were about 0.5 mm/min, while that without mist was about 0.6 mm/min. The suppression in peak burning rates is consistent with the suppression in peak

41
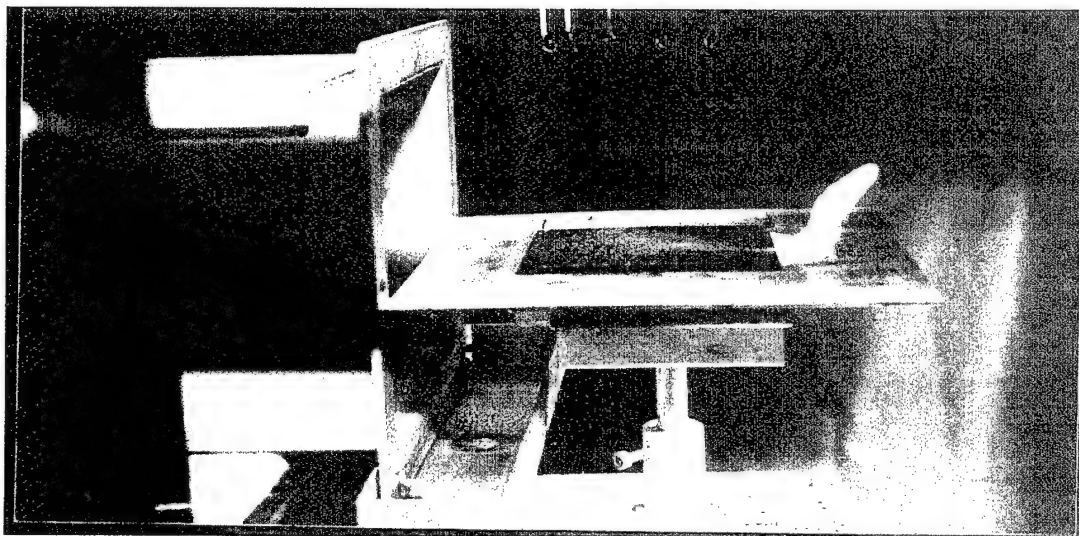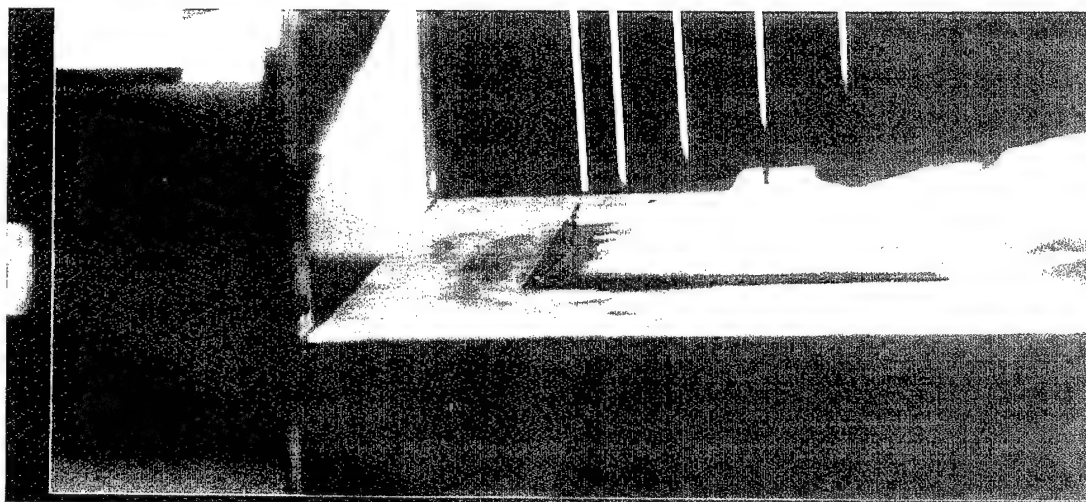
Figure 20: Tests with spray nozzles. (a) Flame being blown off at high mist flow rate; (b) Reduced mist flow rate flame is dislodged and a quench zone is formed. Flame is turbulent.

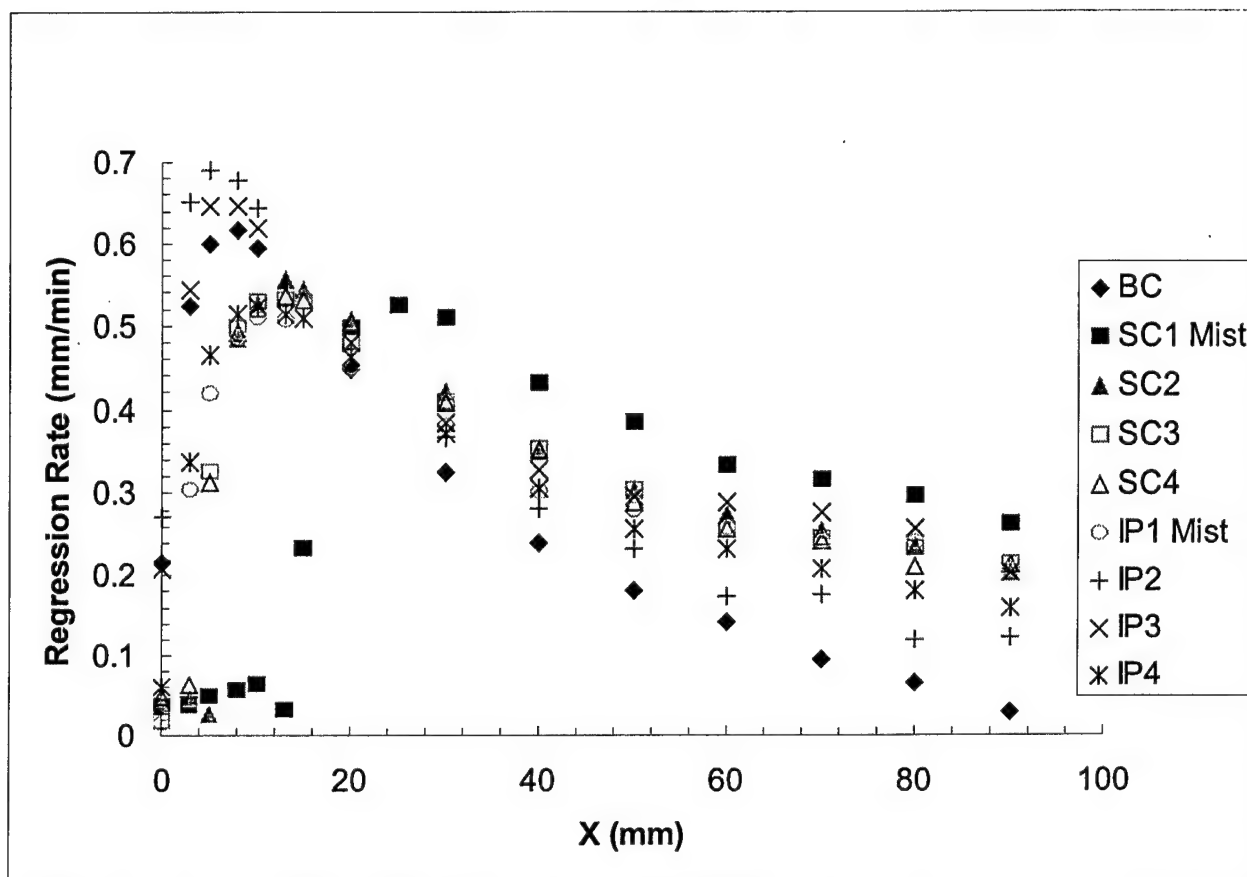**Figure 21:** Burned surface profiles in the (a) base case; (b) mist case IP1 (c) mist case SC3

Figure 22: The effects of mist from pressure atomizing nozzles on local burning rates in 10-minute tests. $U_\infty = 84$ cm/s

temperatures shown in Figs. 9 and 10 (except with IP2 and IP3). The quench distance near the leading edge varied from ~ 2 mm to ~ 25 mm in the various mist tests. Solid cone nozzles had the larger quench distances. These nozzles actually produced the largest mean droplets (Table 2). The SMD for the SC1 and SC2 tests were 47 and 40 μm, respectively. Since significant quench distance and large suppression were obtained in the tests with large droplets, one could speculate that the large droplets could not follow the streamlines at U_∞ of 84 cm/s and probably reached the plate surface in this section due to gravitational effects. Thus direct surface cooling could have played a role here. This speculation is supported by the fact that few drops of water were observed on the quenched zone in the leading section of the PMMA surface in the test with SC1. Because of the quench zone, the X location of the peak regression rate shifted downstream. For example, the regression rate peaked at about X = 13 mm with most of the nozzles, while in the base case it peaked at about X = 8 mm. With SC1 the initial quench zone was as large as 25 mm and the burning rate in the first 16 mm is nearly zero because of the large quench zone. With this nozzle the burning rate peaked even further downstream at about X = 25 mm. With the other nozzles the suppression in the burning rates due to cooling in the first 20 mm is substantial. For example, with SC4 the burning rate at X = 5 mm is about half the base case burning rate at this location.

There is no consistent explanation for results with the IP2 and IP3 nozzles in the leading section. With these nozzles the peak temperatures measured in the leading section (Figs. 9,10) were very close to the base case values and the flame stand off distances were slightly higher in the two mist cases than in the base case. Because of this the temperatures of the flame on the airside are enhanced in these mist cases while on the fuel side the temperatures are suppressed. This temperature profile is not consistent with enhanced burning rate. Therefore, something else could have caused the observed trends.

For X >20 mm the regression rates with mist are higher than the rates without mist and the difference seems to increase with X . The test with SC1 has the highest regression rate at every location in this region and regression rate was enhanced in all the tests with nozzles. At X = 30 mm the highest regression rate was ~ 0.5 mm/min, while the lowest rate was ~ 0.33 mm/min with the base case. On the other hand, at X = 70 mm the highest regression rate was ~ 0.3 mm/min, while the lowest rate of ~ 0.07 mm/min was measured in the base case test. Thus downstream the regression rate was enhanced by as much as a factor of 4 by the addition of mist from SC1. These results are consistent with the downstream temperature profiles presented in Figs. 10-12. We saw that the peak temperatures were suppressed by the addition of mist. However, the temperatures and temperature gradients on the fuel side of the diffusion flame were enhanced when mist was introduced. In addition, the flame standoff distance decreased substantially when mist was added, especially at X = 78 mm. The net effects of all these is that far from the leading edge, the heat feedback to the PMMA surface is enhanced with the introduction of mist from the pressure atomizing nozzles. Therefore, the surface regression rate downstream was enhanced instead of suppressed when mist was introduced.

45

## 3.4 Turbulence and Burning Rate Enhancement Downstream

Since the burning rate enhancement downstream is not obtained in tests with NanoMist, where the mist-induced disturbance was small but rather in tests with pressure atomizing nozzles where the induced disturbance was large, it is plausible that the mist-induced turbulence played a dominant role in the observed burning rate enhancement. Indeed we saw earlier that spray-induced momentum density correlates with flame fluctuations described in terms of dimensionless temperature fluctuations in time θ. This correlation was obtained downstream but not upstream. This is consistent with the enhancement in burning rate measured downstream but not upstream in the tests with pressure atomizing nozzles.

Next, we investigate the correlation between dimensionless burning rate Nux and θ at few points at various regions of the flame. Figure 23 shows Nu_x versus θ at $X = 22, Y = 4$ mm and $X = 78$, $Y = 4$ mm, respectively. The thermal boundary layer is thin in the leading section and hence $X = 22$ mm $Y = 4$ mm is on the airside of the diffusion flame. However, downstream where the thermal boundary layer is thick, $X = 78$ mm $Y = 4$ mm is on the fuel side of the diffusion. The calculated momentum densities induced by the nozzles are written against the various data points. The base case data is included with a momentum density of zero. Two points were included from tests with impingement pin nozzles (IP1 and IP4) and the estimated momentum densities are 8.1 and 29.17 g/cm^2s. Recall that in the impingement pin nozzles, the stream of water leaving the nozzle orifice impinges on a pin in front of the orifice to produce the spray. The estimate of momentum density did not account for this stagnation flow. At $X = 22$ mm burning rate does not correlate with θ. With momentum density of 3.29 g/cm^2s, $\theta \sim 0.05$ while with 2.61 g/cm^2s it is ~ 0.08, implying that lower momentum density induced higher turbulence. There is negligible difference between the burning rates in all the mist cases. The increase in burning rate between the base case and the mist cases is only $\sim 13\%$. At $X = 78$ on the other hand, higher induced turbulence results in larger flame temperature fluctuation and larger burning rates. For example, with momentum density of 2.46 g/cm^2s, $\theta \sim 0.022$, $Nu_x \sim 8.4$ but with momentum density of 3.21 g/cm^2s, $\theta \sim 0.04$ and $Nu_x \sim 11.8$.

Figure 24 shows Nu_x versus θ at $X = 57$ & 78 mm and $Y = 12$ mm. Both locations are on the airside of the diffusion flame. In each plot the corresponding estimated value of droplet momentum density in the wind tunnel is given next to the data point. Figure 24 shows that the burning rate increases with θ. It shows that high momentum density results in large temperature fluctuations downstream and this leads to higher burning rate. Both the tests with solid cone nozzles and impingement pin nozzles show the same trend. The trend is also the same both for $X = 57$ mm and $X = 78$ mm. The only exception is in the test with SC1 where the momentum density is 3.21 gm/cm2 s but the θ and Nu_x are higher than that in the test with SC2 where the momentum density is 3.29 gm/cm2 s. However, the difference between the two momentum densities is small, only $\sim 2\%$. For example, between the base case and SC1 at $X = 78$ mm, the momentum density increased from zero to 3.21 g/cm^2s; θ increased about 6 times and burning rate increased about 6
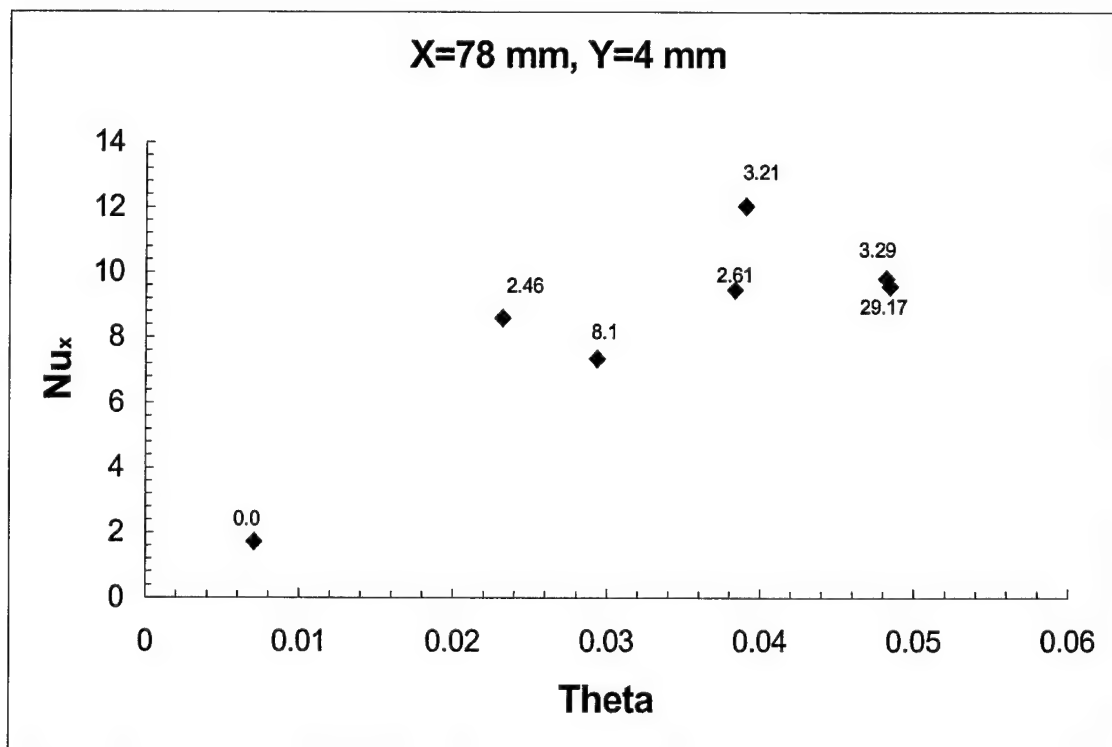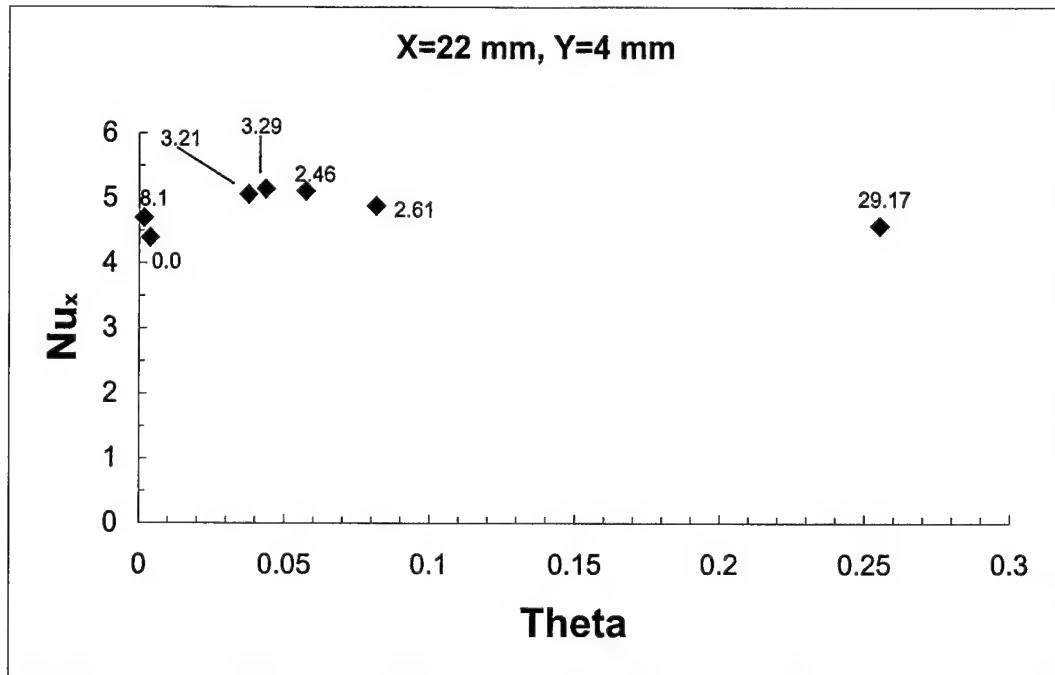
Figure 23: Relation between Nu_x and induced fluctuation θ, at an upstream and down stream location

X=57 mm Y=12 mm

X=78 mm Y=12 mm
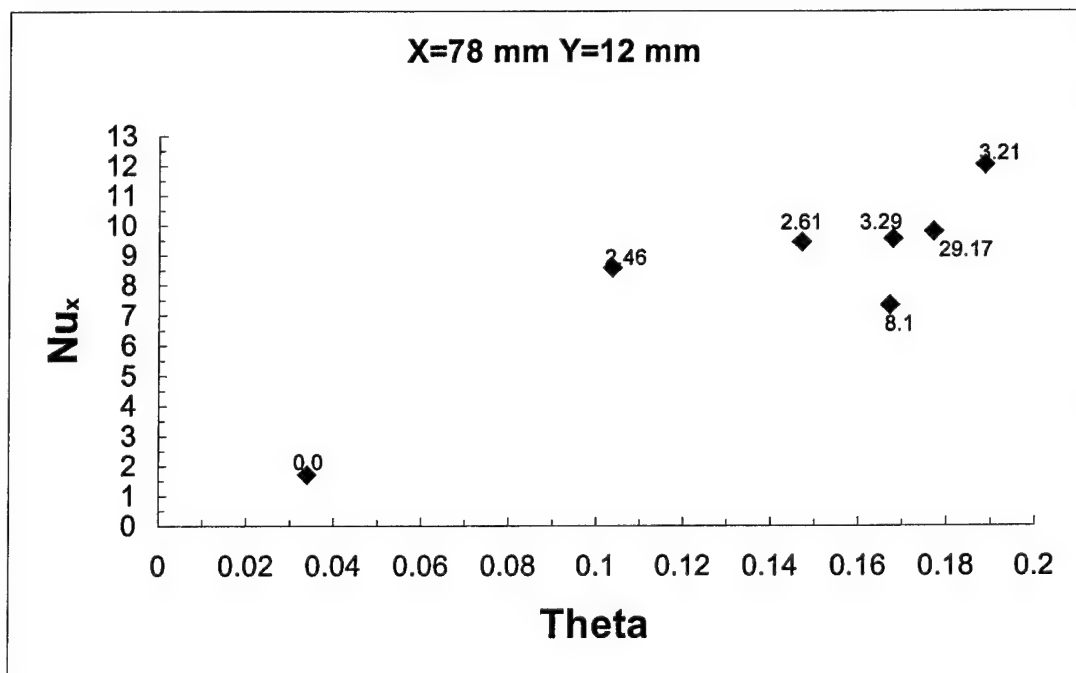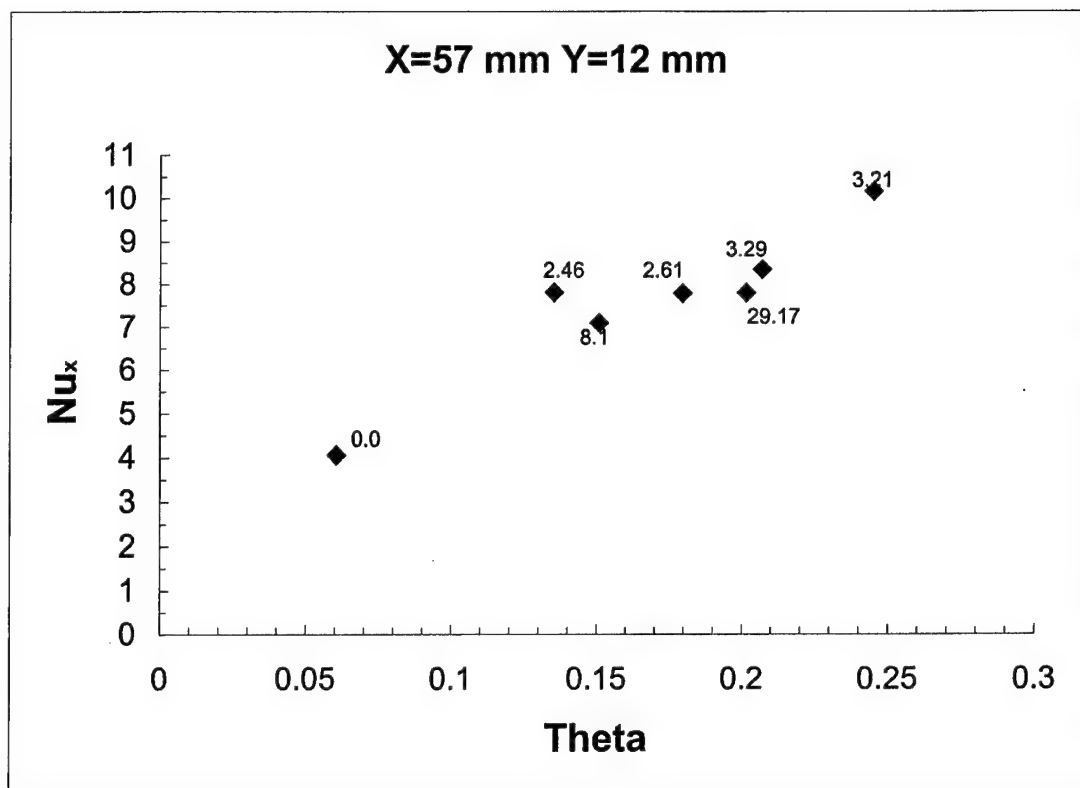
Figure 24: Relation between Nu_x and induced fluctuation θ, in the trailing section

times. Compared to Fig. 21 one notes that change in θ is smaller on the fuel side of the flame than on the airside since the flame is more stable on the fuel side of the diffusion flame [23]. On the other hand, at X =57 mm between the base case and SC1, θ increased about 4 times and burning rate increased about 2.5 times.

The results presented above show that there is a correlation between the spray-induced disturbance, flame temperature fluctuations and enhanced burning rate in the trailing section but not in the leading section. It seems that the disturbance induced by mist injection from the nozzles in the wind tunnel propagates downstream and the flow instability it induced in the boundary layer flame is stronger in the trailing section than upstream. The flame fluctuation in this section, resulted in the flame being brought closer to the plate surface and consequently, the heat feedback to the solid surface increased and the burning rate increased.

The enhancement in burning rate observed in the tests with pressure atomizing nozzles has been shown to correlate strongly with the mist-induced turbulence. As the droplets evaporate in the flame the concentration of water vapor in the flame would go up very significantly compared to the situation without mist. Some earlier workers [9-11] have reported in pool fire experiments that the presence of small concentration of steam enhances the oxidation of carbon and carbon monoxide through the water gas reaction. Atreya et al [11] ran experiments, where liquid water was introduced on the surface of a methane ceramic burner. With a sooty methane flame, they observed an increase in heat release rate at low water application rates and suppression in heat release rate at high water application rates. However, they did not observe similar effects in a blue methane flame. To determine whether the enhancement is as a result of chemical effects or as a result of increased mixing due to the volumetric changes during droplet evaporation, they ran further experiments with methane counter-flow diffusion flame, where water vapor was introduced with the air. Their results show that as water vapor replaced nitrogen in the air, the heat release rate went up. This suggests that water vapor at low concentrations may enhance the combustion reactions in the gas phase. Richard et al. [9] conducted experiments where they burned heptane on a pool of water under a cone calorimeter. The water was heated to boiling point and steam bubbled into the base of the heptane fire. By measuring the carbon dioxide, carbon monoxide, soot and heat release rate with and without steam they deduced that steam addition led to a reduction in soot and carbon monoxide production. They speculated that steam enhanced combustion via the water gas reaction. In the current tests, it is unlikely that the water gas reaction played any significant role in the observed burning rate enhancement downstream. If that was the case we would have observed increase in burning rate in tests with NanoMist, especially at low concentrations. Instead we found that at low concentrations (< 2% mass loading) the burning rate was not enhanced, rather it was suppressed very slightly.

3.4.1 The Effects of Induced Turbulence on Transient Burning Rate Downstream

Since the effects of induce turbulence result in increased heat feedback to the plate surface downstream, it is expected that this will have significant effects on the transient burning rate in the trailing section. We investigate the effects of turbulence on the downstream transient burning rate in a plot of Nu_x versus $Re_x^{0.5}$ in tests with SC3. Figure 25 shows results in 5, 10, 15 and 20-minute tests with and without mist. All the tests were conducted with U_∞ of 84 cm/s. For small $Re_x^{0.5}$ the burning rate is suppressed by mist addition mainly by mist cooling effects, which makes the flame anchor downstream from the leading edge. In this region the base case data show the curvature driven transient burning rate but the mist data do not. This is attributed to the effects of presence of a quench zone near the upstream edge in tests with mist. The timed tests were conducted independently and the exact length of the quench distance cannot be duplicated each time. Thus the Nu_x at various burn-times were not consistent with respect to time.

For large $Re_x^{0.5}$ (downstream), the data show that for each test duration, the local burning rates are significantly higher with mist than without mist. In this section the local burning rate was still increasing up to 20 minute after ignition in the base case tests. However, with mist the burning rate was still increasing up to 5 minutes but, between 10 and 20 minutes the burning rate had reached steady state for $Re_x^{0.5} > 30$. This is clearly shown in the Figure, where the data points cluster around a straight line in this section. Recall that Emmons's steady state prediction and Ananth's [14] steady state numerical solution show a linear relationship. Thus, with pressure atomizing nozzles, the downstream burning rate attains steady state faster than without mist.

To clearly illustrate that the downstream burning rate attains steady state faster with mist than without mist we present in Fig. 26 a plot of Nu_x versus dimensionless time Fo at a typical downstream location ($X = 80$ mm) in tests with and without mist. Clearly, Fig. 26 shows that in the mist case, burning rate increased up to Fo ~ 0.12 (10 minutes) and thereafter reached steady state. However in the base case the burning rate was still increasing up to Fo ~0.24 (20 minutes). Thus, in the trailing section of the PMMA plate because of increased heat feedback as a result of turbulence effects in the mist tests, the plate warmed up faster and steady burning rate was attained faster than in the tests without mist.

Finally the effects of mist on the PMMA burning rates in tests with pressure atomizing nozzles and with NanoMist can be summarized in Fig. 27. Figure 27 shows normalized change in burning rate at each X location versus $Re_x^{0.5}$ in tests with nozzles and NanoMist. In the NanoMist test the mass loading (liquid + vapor) was about 4.3% . The normalized change is obtained as the difference between the burning rate with and without mist divided by the base case burning rate. The negative values represent suppression, while the positive data represent enhancement. The solid cone nozzles SC1, SC2, SC3 and SC4 have droplet momentum densities of 3.21, 3.29, 2.61, and 2.46 g/cm^2 s, respectively, while the impingement pin nozzles IP1, IP2, IP3 and IP4 have momentum densities of 29.2, 25.95, 48.81 and 8.07 g/cm^{2}s, respectively. Fig. 27 shows that burning
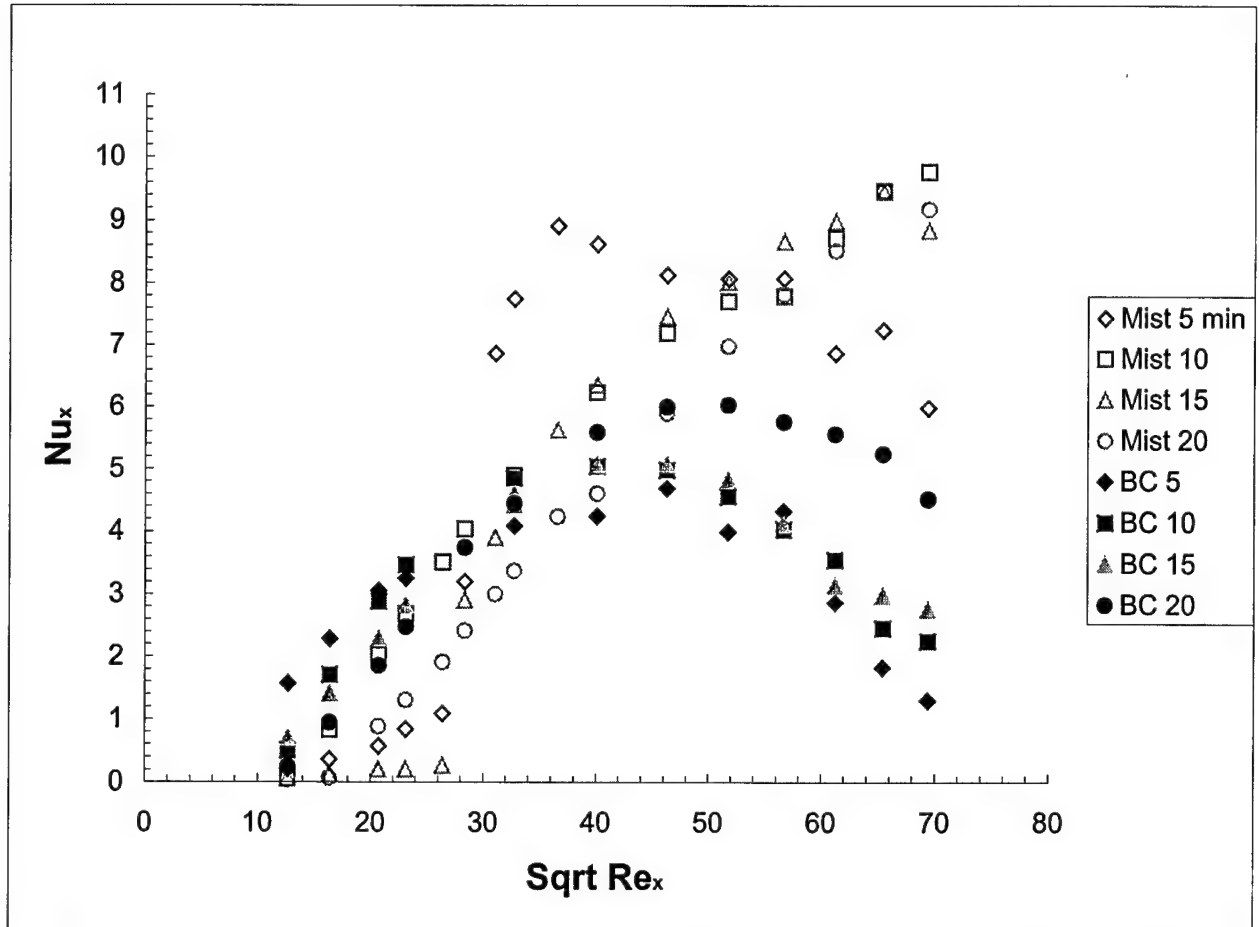
Figure 25: Normalized Burning Rate Nu_x versus $Re_x^{0.5}$ in 5, 10, 15 and 20-minute tests with SC3 and Base case U_∞ =84 cm/s
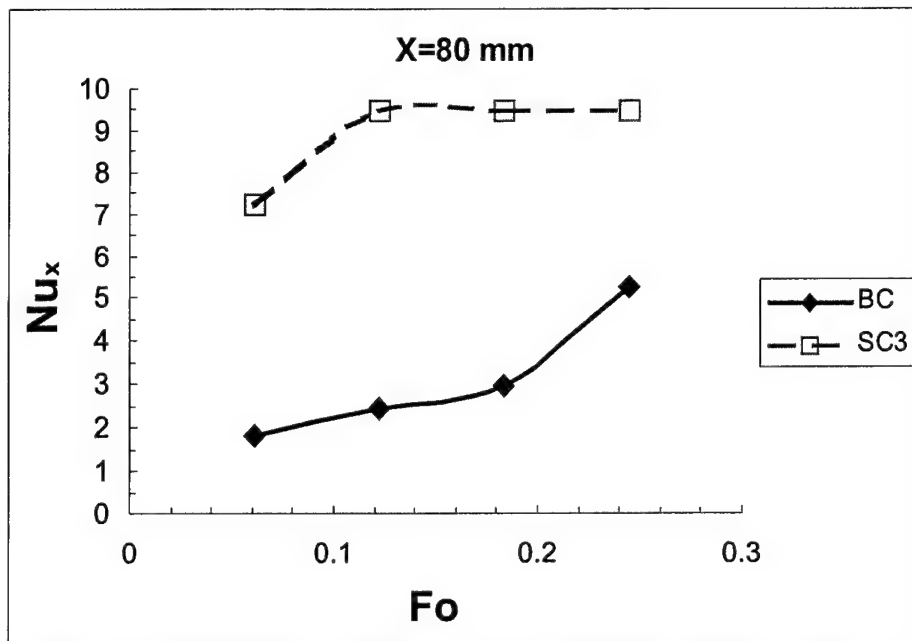
Figure 26: Normalized Burning Rate Nu_x versus dimensionless time Fo downstream in tests with pressure atomizing nozzle SC3 and Base case U_∞ =84 cm/s
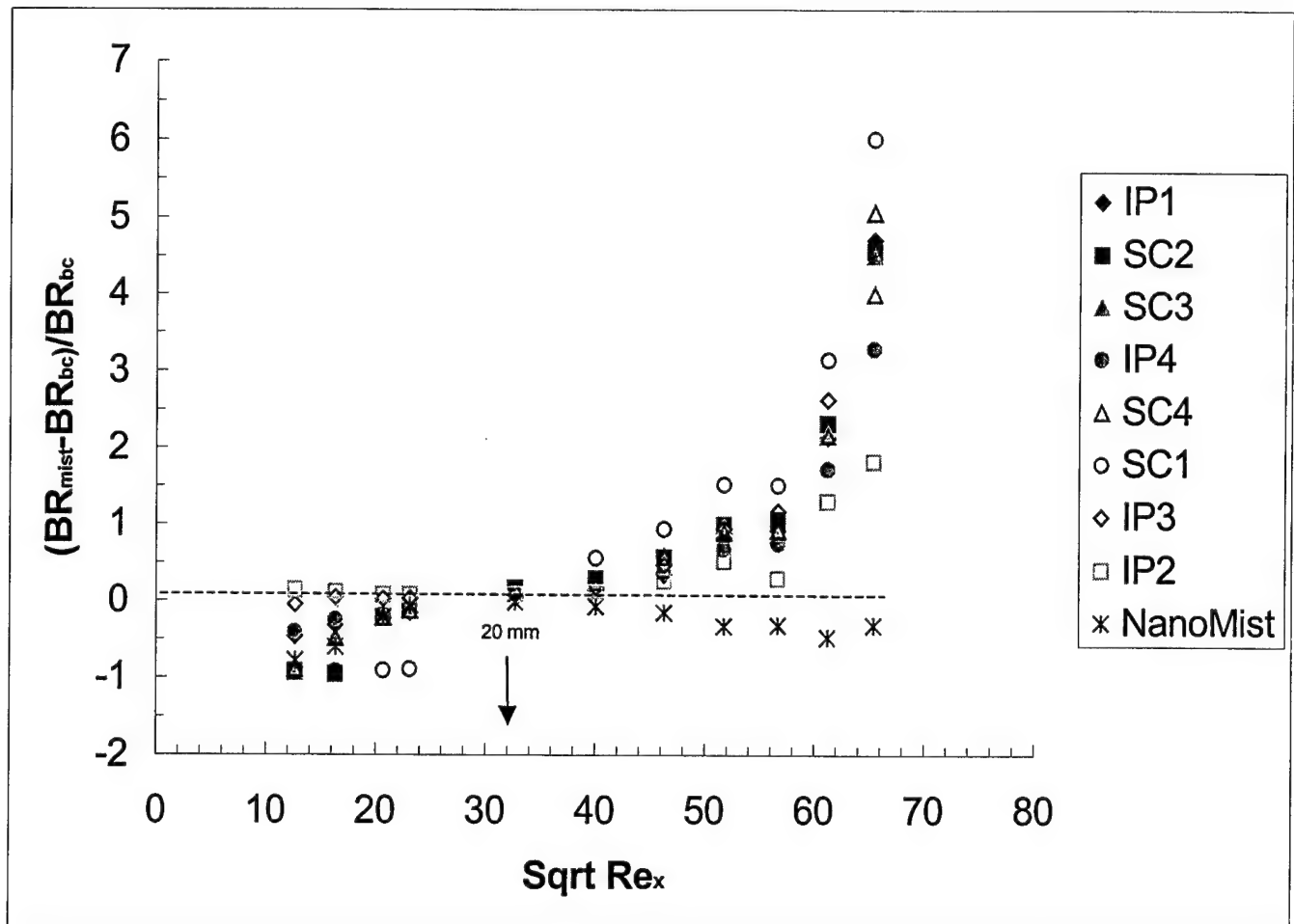
Figure 27: Change in burning rate as a result of mist in 10-minute tests with NanoMist and pressure atomizing nozzles U∞ = 84 cm/s

rate was suppressed in tests with solid cone nozzles and NanoMist for $Re_x^{0.5} <32$, which corresponds to the leading 20 mm of the plate. The IP nozzles show no significant suppression in this region. However for $Re_x^{0.5} >32$ (X > 20mm) the burning rate was enhanced in tests with all the nozzles but it was suppressed in the NanoMist tests. In the leading section, burning rate was suppressed by as much as 80% with the nozzles and slightly less with NanoMist. With NanoMist burning rate was suppressed downstream by as much as 30%. However, with SC1, which has a high-induced momentum on the droplets, the burning rate was enhanced by as much as 6 times near the PMMA trailing edge. It is also interesting to note in Fig. 27 that burning rate enhancement increased sharply for $Re_x^{0.5} >50$. Burning rate is enhanced by about 100% between $30 <Re_x^{0.5} <52$ (20 <X <60 mm) but it is enhanced by about 5 times between $52 <Re_x^{0.5} <65$ (60 <X <80 mm). Thus Fig. 27 further confirms the strong correlation between the nozzle-induced turbulence, which is most significant downstream and the enhanced local burning rate measured in tests with pressure atomizing nozzles.

3.5 Mist Transport

The above discussions have detailed how the water mist injected into the airflow at the mist chamber (Fig. 1) affected the PMMA boundary layer combustion. However, not all the mist introduced at the injection point reach the tunnel exit as air-borne droplets. Some of the droplets hit the tunnel surface and adhere to the surface and form puddles of water. Some large droplets may fall to the tunnel floor due to gravity. In Table 2 we listed the measured water mass fraction at the tunnel exit for the mist cases for which suppression experiments were conducted. Additional tests were conducted at other water pressures, number of NanoMist piezoelectric discs and tunnel flow velocities to study the transport of water droplets through the tunnel. A summary of the data is shown in Table A1 in the Appendix. For the spray nozzles, water pressure was varied between 2.81 kg/cm^2 (40 psi) and 456.95 kg/cm^2 (650 psi). NanoMist output was increased five fold by increasing the number of discs energized. Tests were conducted at airflow velocities of 60, 84, 120 and 168 cm/s.

Figure 28 shows the output water mass fraction versus the input water mass fraction. Input mass fraction is water injection rate divided by the air flow rate in the tunnel while the output is the difference between the input and the collected losses. In this discussion loss is used to describe water drained from the tunnel floor during the test plus water cleaned off the tunnel walls at the end of the test. Thus the output mass fraction includes water vapor resulting from droplet evaporation from the injection point to the tunnel exit. For NanoMist the output is a linear function of the input and the data fit y = 0.9233x very well. Thus at high or low NanoMist concentrations the losses in transporting the mist through the tunnel is less than 8%. The length of the tunnel for the NanoMist tests was 152.4 cm. Since the tunnel cross section is 15 x 15 cm, this loss was incurred on ~ 9144 cm^2. It seems that increase in the tunnel air velocity makes no difference in the amount of mist lost along the channel. This is another indication that the droplets follow the streamlines even at low tunnel velocities because they are very tinny.
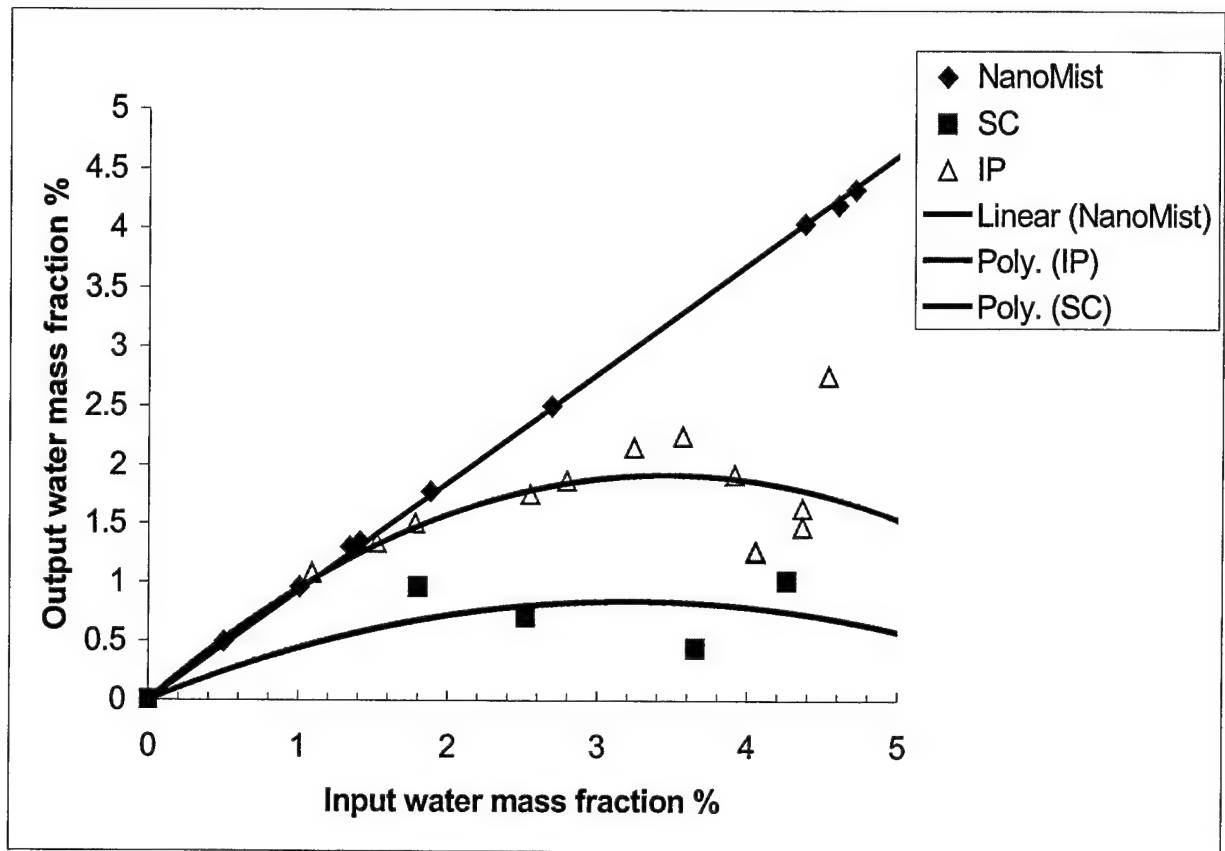
54

Figure 28: Water mass fraction introduced into the wind tunnel versus air-borne water mass fraction at the exit of the tunnel for SC and IP nozzles and NanoMist

This is a major advantage of NanoMist over spray nozzle mist. The data for the impingement nozzle IP tests show a deviation from the straight line after input mass fraction of about 1.0. At high input mass fraction the data show a lot of scatter and seems to be approaching a constant value. The three points in the linear portion of the curve were for tests at 120 and 168 cm/s. At high velocities the air tends to drag the droplets along and the losses are less. At high input concentrations (>4) the data that fall below the curve are for tests at 84 cm/s and low pressures where the droplets are large and were not easily carried in the airflow. The data with solid cone SC (60° spray angle) nozzles have a large scatter. At a given input the output is the least of the three categories. For example at an input mass fraction of about 2.5%, the SC nozzle output is ~1/3 that of the IP nozzles and ~ ¼ that of the NanoMist. The SC nozzles were run at the least pressure and they produced droplets that are more than twice as large as those from IP nozzles and ~14 times larger than NanoMist. Figure 28 shows that NanoMist transport through the tunnel has the least mist loss. It has about 10 times less loss than the SC nozzles for input water mass fraction greater than 4. The tests with nozzles were conducted with a shorter wind tunnel because of reasons explained earlier. The tunnel length was 106.7 cm and so the losses were over a surface area of 6402 cm^2 (compared to 9144 cm^2 for NanoMist). The data in Fig. 28 compares the transport of PAN mist and NanoMist in the wind tunnel used in the current experiments. A more general description of the mist transport in terms of dimensionless parameters based on detailed tests and analysis is needed. This would reveal the role of various design parameters on the transport of mist droplets through an enclosure.

4.0 CONCLUSIONS

In the preceding section results of experiments to investigate the effects of air-borne water mist on the burning rate of a forced convection boundary layer flame over PMMA were presented. Fine water droplets with SMD < 50µm were injected into the incoming airflow at U_∞ = 84 cm/s. Mist with 10µm <SMD<50 µm was sprayed co-currently into the wind tunnel from pressure atomizing nozzles. NanoMist with SMD ~ 3µm was introduced from an ultrasonic mist generator. The time-averaged local burning rates were measured and gas phase temperature profiles were mapped in tests with and without water mist. Analysis of the results shows the following trend:

1. NanoMist seems to evaporate before reaching the flame front. Therefore, in the leading section of the plate NanoMist suppressed burning rate mainly as a result of gas phase cooling. Extinguishment was obtained by flame blow off and the stability window is narrow. With 84 cm/s inlet velocity extinguishment was obtained for NanoMist mass loading > 4.3% (liquid + vapor) and negligible suppression was obtain with lower mass loading. With nozzles, the droplets were bigger and it seems they evaporate closer to the initial flame anchor location and the rapid cooling effects led to the formation of a quench zone near the leading edge. At U_∞ of 84 cm/s the length of the

quench distance varied from about 2 mm to 25mm. Flame extinguishment was obtained by the extension of the quench distance and eventual blow off rather than by the cooling and shrinking of the flame.

2. The local burning rate in the leading section is transient with and without mist because of the moving boundary effects. However because of the cooling effects of mist and formation of quench zone the burning rate at a given time is less with mist than without mist.

3. In the trailing section of the plate burning rate was slightly suppressed (~ 40%) in tests with 4.3% NanoMist and much less suppression was obtained at lower concentrations. In this section the burning rate is transient with and without mist. This is as a result of low heat feedback and slow in-depth heat transfer in this section. Since the rapid evaporation of NanoMist cools the gas phase, the heat feed back to the solid in Nanomist test is even less than with the base case, hence its burning rate increases at a slower rate and the transient lasts longer.

4. In tests with pressure atomizing nozzles the burning rate downstream is enhanced instead of suppressed by the addition of mist. It seems that the mist induced flame fluctuation brought the flame closer to the plate surface, increasing heat feedback to the surface. This led to enhanced burning rate. The results show a correlation between the injection momentum density of droplets, the fluctuation in flame temperature in the trailing section and the enhanced plate regression rate. With a momentum density of about of 3 g/cm^2s the burning rate was enhanced about 5 times in the trailing section.

5. With the nozzles, the burning rate downstream is also transient. However, unlike with NanoMist, steady state is approached faster in this case because of the higher heat feedback to the solid surface (compared to the base case) as a result of mist-induced turbulence.

6. A study of the mist transport through the current wind tunnel reveal that with NanoMist, losses along the tunnel were less than 8% of the input concentration, while with nozzles the losses were much higher. They are as much as 10 times higher with solid cone nozzles with input mass loading greater than 4.0

5. ACKNOWLEDGEMENTS

6. REFERENCES

1. Rasbash, D.J., Rogowski, Z.W., and Stark, G.W.V. " Mechanism of extinction of liquid fires with water sprays" *Combustion and Flame*, 4 :223 (1960).
2. Downie, B, Polmeropoulos, C and Gogos G. "Interaction of a water mist with a buoyant methane diffusion flame" *Fire Safety J.* **24** p.359 (1995)
3. Ndubizu C.C, Ananth, R and Tatem P.A "The effects of droplet size and injection orientation on water mist suppression of low and high boiling point liquid pool fires" *Combust. Sci. and Tech* **157**: 63-86 (2000)
4. Kokkala, MA "Fixed water spray against open liquid pool fires" VIT Research Report #696 Technical research center of Finland Espoo, Finland. (1990)
5. Mawhinney J. R "Characteristics of water mist fire suppression in enclosures" Proceedings of the Halon Alternative Technical Working conference, Albuquerque, N.M (1993)
6. Ndubizu, C.C; Ananth,R.; Tatem, P.A; and Motevalli, V; "On Water mist fire suppression mechanisms in a gaseous diffusion flame" *Fires Safety J.* **31:3** p.253 (1998)
7. Seshadri, K "Structure and extinction of laminar diffusion flame above condensed fuels with water and nitrogen" *Combustion and Flame* **33**:197(1978).
8. Lentati, A.M and Chelliah, H.K; "The dynamics of water droplets in a counterflow field and its effects on flame extinction" Fall Technical Meeting, The Eastern States section of the Combustion Institute, Hilton Head, SC Dec. 9-11 (1996).
9. Richard J.; Garo, J.P; Souil, J.M Vantelon, J.P and Knorre, V.G "Chemical and physical effects of water vapor addition on diffusion flames" *Fires Safety* J **38** (2003) pp 569-587
10. Yao, B; Fan, W and Liao G "Interaction of water mists with a diffusion flame in a confined space" *Fire Safety J.* **33** 129-139. (1999)
11. Atreya A., Crompton T. and Suh J. "A study of the chemical and physical mechanisms of fire suppression by water" Proceedings of sixth International symposium on fire safety science 5 –9 July 2000. University of Poitiers, France p. 493-504
12. Tamanini, F., "A study of the extinguishments of vertical wood slabs in self-sustained burning by water spray application" *Combust. Sci. and Tech* **14**: 1-15 (1976)
13. Magee, R.S and Reitz, R.D "Extinguishment of radiation augmented plastic fires by water mist" *Proc Combust. Inst.* **15**: 337-347 (1975)
14. Ananth R ; Ndubizu C C and Tatem P.A "Burning rate distributions for boundary layer flow combustion of a PMMA plate in forced flow" *Combustion and Flame* **135** (2003) pp 35-55
15 Ndubizu, C.C; Ananth,R.; Tatem, P.A "Transient burning rate of a non-charring plate under a forced flow boundary layer flame" Paper submitted for publication in *Combustion and Flame.(2004)*

16. Zhuo L and Fernandez-Pello A.C "Turbulent burning of a flat fuel surface" *Fire Safety Science: Proceedings of the Third International Symposium,* Hemisphere. Washington D.C pp. 414-424 (1990)

17. Ahmad T and Faeth G.M "Turbulent wall fires " *Proc. Combust* **17** pp.1149 (1978)

18. Sivathanu Y , Oke, H.P; Fu, C; Wang,A and Sojka P.E "Droplet interaction with hot surfaces" Technical Report for NGP BFRL NIST En'Urga Inc March 2000

19. Adiga, K. C. and Adiga, R,. "Method and device for production, extraction and delivery of mist with ultra fine droplets," U.S Patent Publication 20030127535

20. Vovelle C,: R Akrich; J.L Delfau and S Gresillaud. "Influence of the thickness on the thermal degradation of PMMA" *Fire Safety Science: Proceedings of the First International Symposium,* Hemisphere. Washington D.C (1986) pp.473

21. Tewarson A., and Pion R.F., *Combustion and Flame* **26** (1976) :85

22. Ndubizu C ; Ananth R ; Tatem P A " Boundary layer flame spread over PMMA within the quench zone: A moving boundary effect" *Combust. Sci. Tech.* **175**:1 p.1-26 (2003)

23. The Temperature Handbook, Vol. 29; Omega Engineering Inc. (1995) pp. Z159

24. Ahmad T and Faeth G.M "Investigation of the laminar over fire region along upright surfaces" *J. Heat Transfer* **100** (1978) 112-119

25. Emmons, H.R., Zeit. Fur Angew. Math. and Mech. **36** (1956):60

26. Tewarson A, "Generation of heat and chemical compounds in fires" In *SFPE Handbook of Fire Protection Engineering.* P.J. DiNenno et. al (Eds.). National Fire Protection Association, Quincy, MA (1995) p. 3-68

27. Ndubizu C C Ananth R and Tatem P.A "The burning of a thermoplastic material under a forced-flow boundary layer flame" Naval Research Laboratory Memorandum report NRL/MR/6180-02-8630 (2002)

28. Ananth R; C.C Ndubizu and P.A Tatem "Pyrolysis and boundary layer combustion of a non-charring solid plate under forced flow" Naval Research Laboratory Memorandum report NRL/MR/6180-03-8700 (2003)
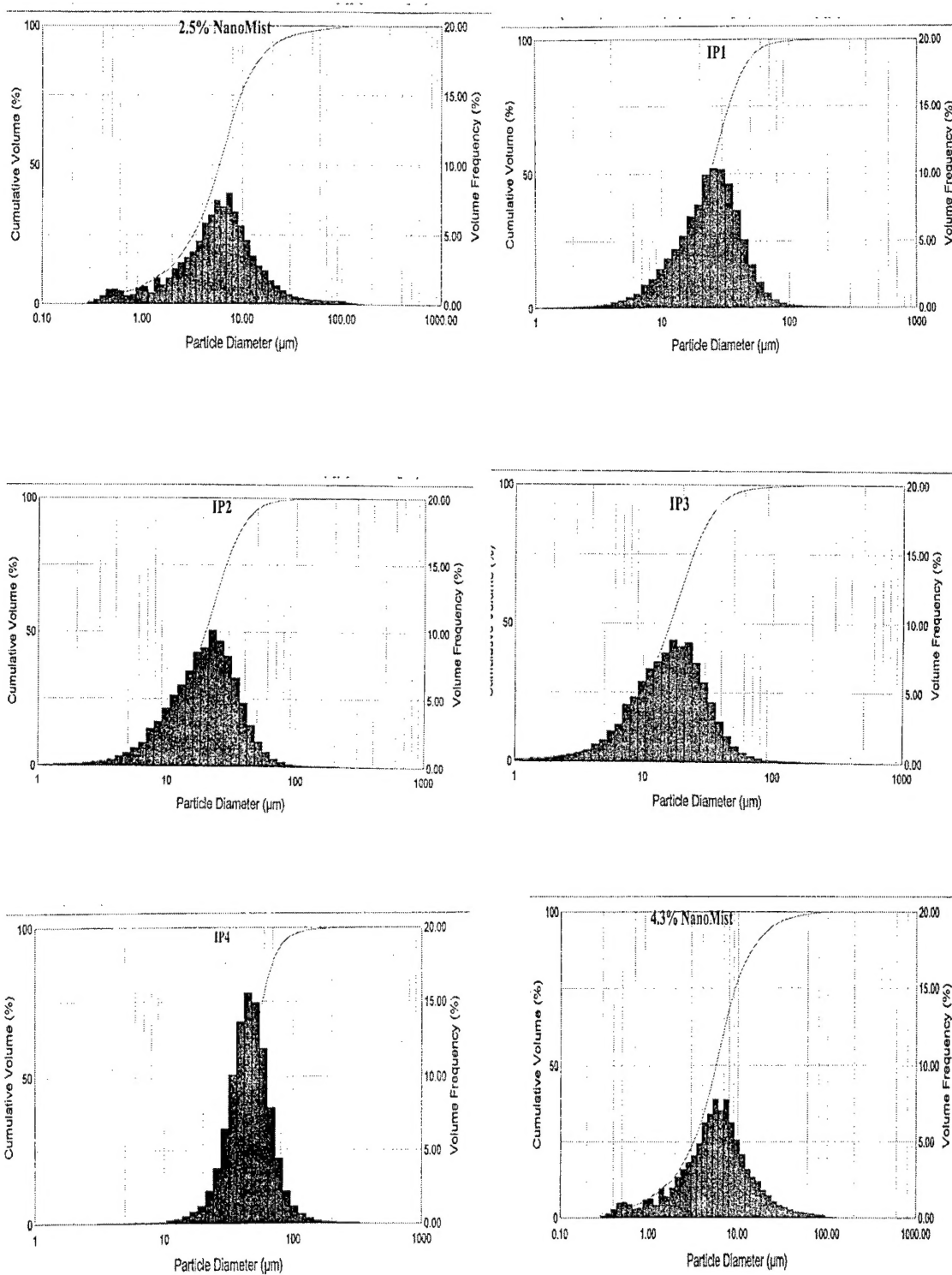
APPENDIX
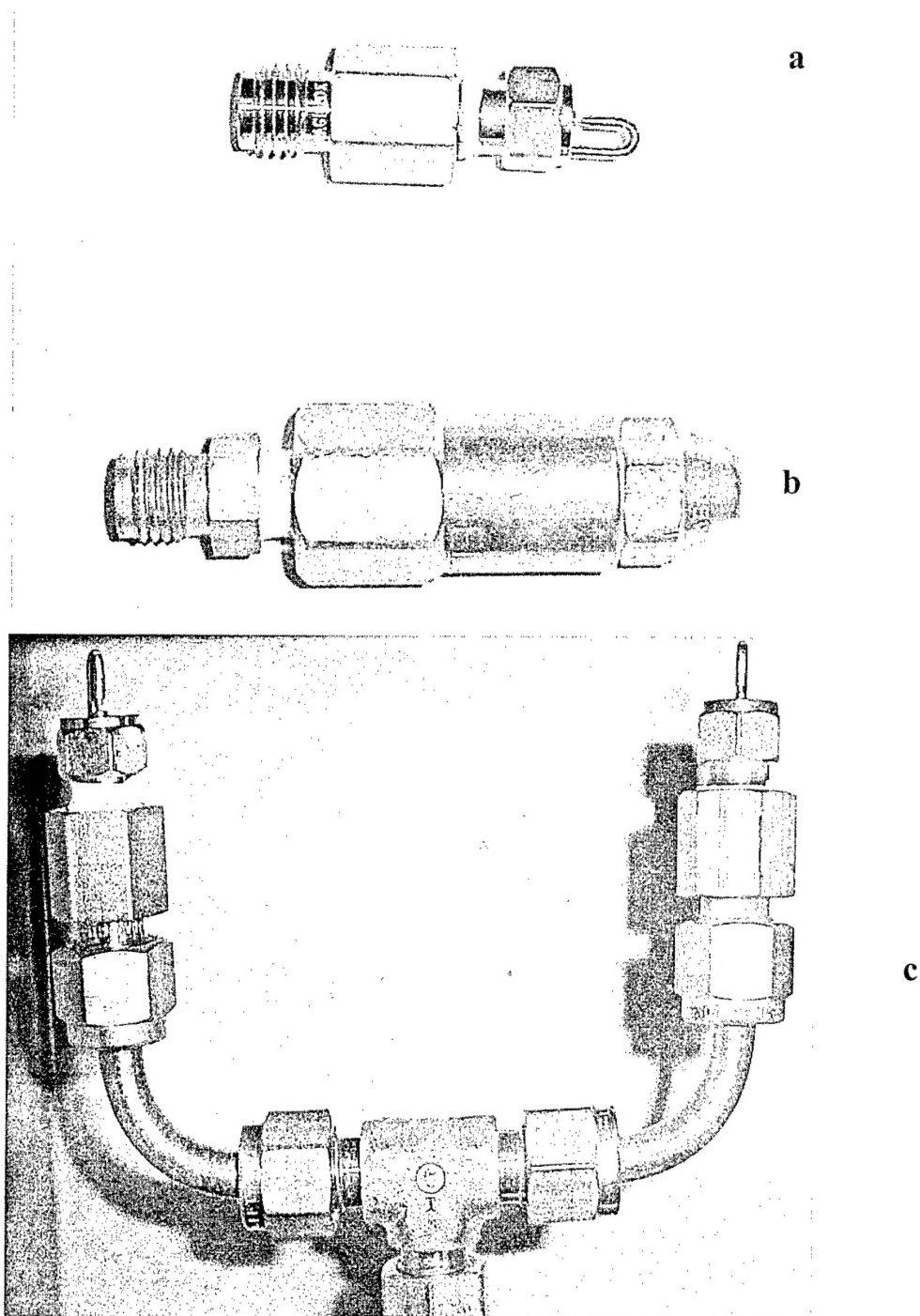
Figure A1: Picture of Spray nozzles used in the tests – (a) Impingement pin nozzle;
(b) Solid cone nozzle; (c) Arrangement of two IP nozzles (IP1) for higher mist flow
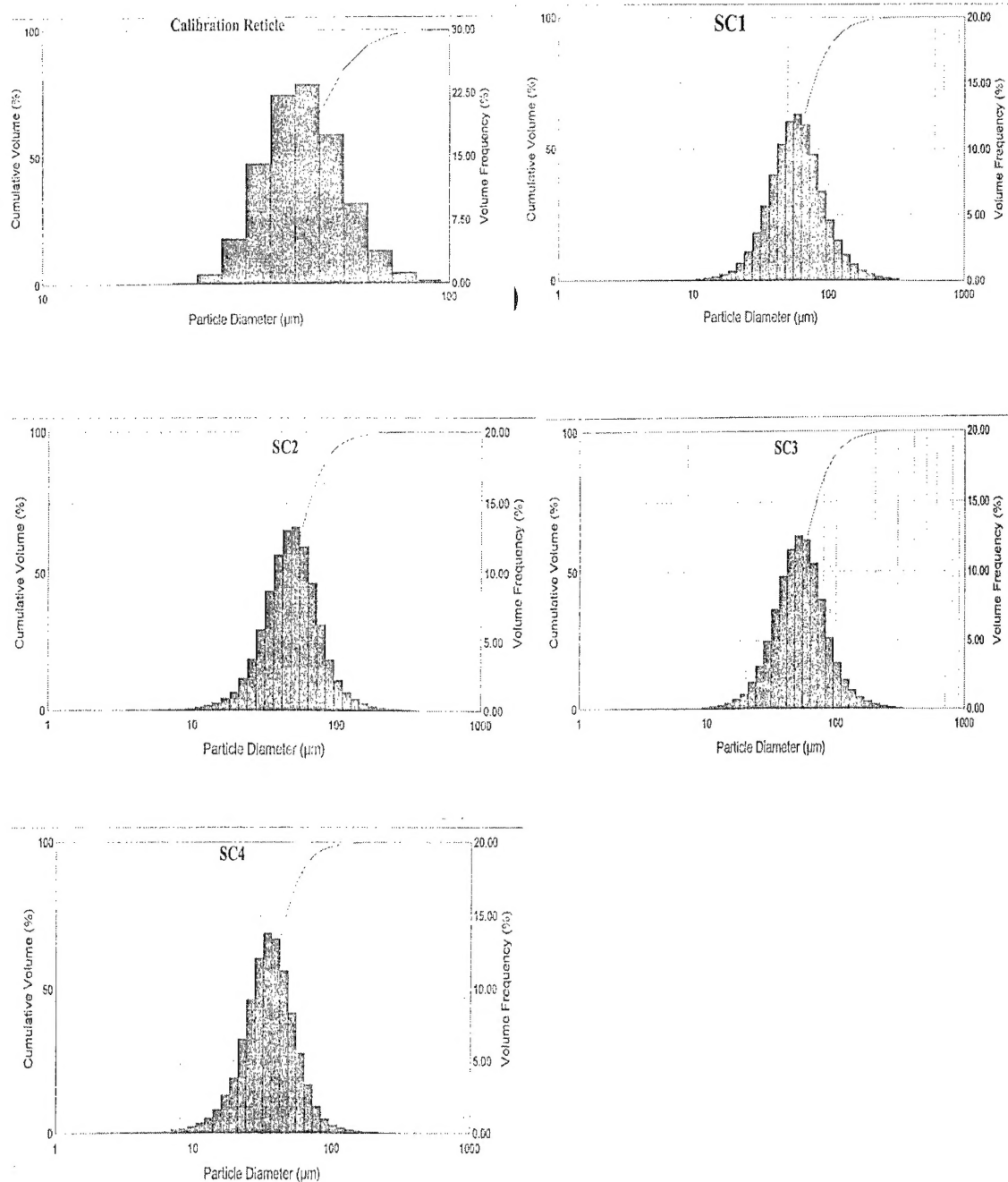
Figure A2: Droplet Diameter distributions for the Reticle,
SC1,SC2,SC3 and SC4 tests

Figure A3: Droplet diameter distributions for tests with 2.5% NanoMist, IP1, IP2, IP3, IP4 and 4.3% NanoMist

Table A1: MIST TRANSPORT THROUGH THE TUNNEL

Nozzle	U cm/s	Water Flow Rate g/min	Loss g/min	Water mass fraction at exit %	% Loss %	SMD Microns	Input Mass Fraction %	Loss mass Fraction %
NanoMis	84	47.2055	3.7475	4.33	7.93869	3.16	4.714051	0.374234
3	84	26.9745	2.0515	2.5	7.60533	3.15	2.693736	0.2048675
1	84	13.487	0.4	1.3	2.96582	3.24	1.346843	0.0399449
4	84	46.0538	3.6468	4.2	7.91856	3	4.599039	0.3641779
3	120	26.974	1.591	1.774	5.89827	2.66	1.88558	0.1112167
2	120	20.23	1.0175	1.344	5.02966	2.66	1.41415	0.0711269
2	168	20.23	1.0175	0.959	5.02966	2.84	1.010107	0.050805
1	168	10.115	0.153	0.497	1.51261	3.11	0.505054	0.0076395
2.6	120	26.975	1.61	1.773	5.96849	2.77	1.88565	0.1125448
5	84	43.834	3.381	4.04	7.71319	3.19	4.377365	0.3376345
SC1	84	48.8	35.098	1.368	71.9221	47.35	4.873281	3.5049677
SC2	84	42.7	32.63	1.01	76.4169	39.71	4.264121	3.2585075
SC3	120	36.1	26.001	0.7059	72.0249	46.11	2.523521	1.8175641
SC3	60	36.1	32.08	0.562	88.8643	37.3	5.047042	4.4850165
SC3	168	36.1	16.9	0.959	46.8144	44.78	1.802515	0.8438366
SC3	84	36.61	31.675	0.44	86.5201	43.14	3.65596	3.163139
SC4	84	24.28	13.668	1.06	56.2932	28.25	2.424657	1.3649182
IP1	84	43.72	27.361	1.63	62.5823	16.4	4.365981	2.7323329
IP1_250	84	40.6	27.93	1.265	68.7931	19.71	4.05441	2.7891546
IP1_250	84	40.6	28.03	1.255	69.0394	18.09	4.05441	2.7991408
IP1	84	43.72	28.98	1.47	66.2855	17.21	4.365981	2.89401
IP1	120	21.86	2.776	1.334	12.699	19.32	1.528093	0.1940525
IP1	168	21.86	0.224	1.079	1.0247	20.17	1.091495	0.0111846
IP2	60	25.5	9.44	2.245	37.0196	11.93	3.565085	1.3197804
IP2	120	25.5	3.976	1.504	15.5922	15.14	1.782542	0.2779368
IP2_500	84	28	9.3	1.867	33.2143	11.52	2.796145	0.9287196
IP2_500	60	28	14.276	1.919	50.9857	10.64	3.914603	1.9958883
IP2	84	25.55	7.959	1.75	31.1507	13.2	2.551482	0.7948042
IP3	60	32.45	12.744	2.755	39.2727	9.41	4.536745	1.7817036
IP3	84	32.45	10.842	2.15	33.4114	10.9	3.240532	1.0827073
IP4	84	25.1	16.553	0.85	65.9482	38.28	2.506544	1.653021
IP4	60	25.1	20.46	0.649	81.5139	33.42	3.509162	2.8604563